



HAL
open science

Tridimensional nonhydrostatic transient rip currents in a wave-resolving model

Patrick Marchesiello, Francis Auclair, Laurent Debreu, James C. McWilliams, Rafael Almar, Rachid Benshila, Franck Dumas

► **To cite this version:**

Patrick Marchesiello, Francis Auclair, Laurent Debreu, James C. McWilliams, Rafael Almar, et al.. Tridimensional nonhydrostatic transient rip currents in a wave-resolving model. 2020. hal-02883697v1

HAL Id: hal-02883697

<https://inria.hal.science/hal-02883697v1>

Preprint submitted on 29 Jun 2020 (v1), last revised 29 Mar 2021 (v3)

HAL is a multi-disciplinary open access archive for the deposit and dissemination of scientific research documents, whether they are published or not. The documents may come from teaching and research institutions in France or abroad, or from public or private research centers.

L'archive ouverte pluridisciplinaire **HAL**, est destinée au dépôt et à la diffusion de documents scientifiques de niveau recherche, publiés ou non, émanant des établissements d'enseignement et de recherche français ou étrangers, des laboratoires publics ou privés.

Tridimensional nonhydrostatic transient rip currents in a wave-resolving model

Patrick Marchesiello^{a,*}, Francis Auclair^d, Laurent Debreu^e, James McWilliams^c, Rafael Almar^a, Rachid Benshila^b, Franck Dumas^f

^a*IRD/LEGOS, Toulouse, France*

^b*CNRS/LEGOS, Toulouse, France*

^c*University of California, Los Angeles, USA*

^d*LA, University of Toulouse, France*

^e*Univ. Grenoble Alpes, Inria, CNRS, Grenoble INP, LJK, 38000 Grenoble, France*

^f*SHOM, Brest, France*

Abstract

Flash rips and surfzone eddies are transient horizontal structures of order 10-100 m scale, that can be generated in the surfzone in the absence of bathymetric irregularities. They are traditionally assessed within a depth-averaged framework that involves intrinsic horizontal shear instabilities or/and direct short-crested wave vorticity generation. In this paper, we revisit surf eddy generation processes with a new tridimensional, wave-resolving model (CROCO). We first present a quick overview of a free-surface, compressible approach adapted to nearshore dynamics. Its ability to simulate surface gravity wave propagation and nearshore breaking is validated against laboratory experiments. Next, we present a full 3D, wave-resolving real-case simulation of nearshore currents in Grand Popo Beach, Benin, forced by waves with frequency and directional spreading. The generation of surfzone eddies by the 3D model is shown to differ considerably from that produced by depth-averaged models, owing to the vertical structure of currents produced by shallow breaking that prevents a strong inverse energy cascade. Processes of both horizontal shear instability and short-crested wave breaking are restricted. Instead, the vertical shear flow is prone to forced variability by wave groups and to a Kelvin-Helmholtz-type instability. The latter shows primary and secondary instabilities, that generate spanwise and streamwise vorticity connecting breaking-induced rolls to larger horizontal surfzone structures. Streamwise filaments, appearing as ribs or mini rips, can extend beyond the surfzone but with lower energy than depth-averaged model rips

(offshore mean EKE is reduced by a factor 2). Energy spectra and visual inspections of tracer and sediment concentration shows much better fit between the 3D model patterns and in-situ and aerial observations in Grand Popo Beach. Our results thus suggest that nearshore vortical motions are driven by nonhydrostatic dynamics, at least for moderate wave forcing.

Keywords: surfzone, transient rip, 3D instability, nonhydrostatic, wave-resolving model

1. Introduction

Flash rips and surfzone eddies are generally defined as transient horizontal structures of size ranging between water depth and surfzone width, i.e., of order 10-100 m, which are generated in the surfzone in the absence of bathymetric irregularities. They are studied separately from stationary rip currents confined to deeper channels between sandbars (Marchesiello et al., 2015). They are also separated from breaking-induced rollers that scale with wave height (Cox and Anderson, 2001), and even smaller vortices of the fully developed turbulent bore (Svendsen and Madsen, 1984). However, the separation between surf eddies and turbulence is uncertain (Longo et al., 2002) and the possibility of intermediate scales and processes linking horizontal and vertical vorticity generation has been suggested — e.g., Short et al. (1993) describing ephemeral and shallow *mini rips* over Australian low tide terrace beaches — but not clearly demonstrated.

Because it is difficult to sample transient rip currents with sufficient spatial resolution (Henderson et al., 2017), our concepts largely rely on numerical models, mostly depth-averaged models. Three types of processes stand out:

- Horizontal (2DH) shear instability of longshore currents
- Short-crested wave vorticity generation (here called Peregrine process)
- Tridimensional (3D) shear instability

*Corresponding author

Email address: `patrick.marchesiello@ird.fr` (Patrick Marchesiello)

19 Horizontal shear instability of longshore currents is the earliest process of eddy gener-
20 ation, accounting for the intrinsic variability of wave-driven currents (Bowen and Holman,
21 1989; Dodd et al., 1992; Allen et al., 1996; Slinn et al., 1998; Özkan-Haller and Kirby, 1999;
22 Dodd et al., 2000; Uchiyama et al., 2009). This process was typically studied with wave-
23 averaged shallow-water models, where momentum transfer from wave to current fields is
24 entirely parametrized. Its importance has faded during the last decade due to prevalence of
25 the Peregrine process, but also to conflicting results given by newly developed wave-averaged
26 tridimensional models (Newberger and Allen, 2007; Splinter and Slinn, 2003).

27 The second process, largely due to Peregrine (1998), is the current nearshore community
28 views of driving mechanisms for wave-averaged circulation in the surfzone (Kirby and De-
29 rakhti, 2019). Boussinesq equations for weakly dispersive intermediate and shallow water
30 waves provides a conceptual model for the action of spatially varying wave breaking, i.e.,
31 short-crested waves (Johnson and Pattiaratchi, 2006; Bonneton et al., 2010; Feddersen et al.,
32 2011; Clark et al., 2012; Feddersen, 2014). In this model, small vortices result from gener-
33 ation by differential breaking, and combine over time into larger eddies through an inverse
34 cascade mechanism, consistent with 2D turbulence. The surfzone is thus a production center
35 for eddies with scales roughly ranging from 10 to 100 m. In addition, the coastal boundary
36 imposes that eddies and associated filaments can only go offshore, providing a mechanism
37 for enhanced cross-shore dispersion of various tracers.

38 The theoretical framework from depth-integrated models neglect the effect of verti-
39 cal shear. Following the advent of robust 3D formulations of wave-averaged equations
40 (McWilliams et al., 2004; Ardhuin et al., 2008), a number of 3D modeling studies have
41 emerged in the last decade (Newberger and Allen, 2007; Uchiyama et al., 2010; Kumar
42 et al., 2012; Marchesiello et al., 2015; Uchiyama et al., 2017; McWilliams et al., 2018; Akan
43 et al., 2020). They show a modulation of nearshore circulation when wave breaking occurs
44 in a shallow surface layer. However, short-crested wave breaking is generally neglected in
45 these wave-averaged studies (or addressed in ad-hoc manners) and all real-scale applications
46 to date are performed using hydrostatic assumption, thus neglecting horizontal vorticity
47 motions.

48 Nonhydrostatic dynamics are essential in our third listed process of surf eddy generation.
49 They are mostly studied in laboratory experiment (Nadaoka et al., 1989) and laboratory-
50 scale Large-Eddy Simulations (LES) using 2.5D CFD models applied to individual wave
51 breaking (Lin and Liu, 1998; Watanabe and Saeki, 1999; Watanabe et al., 2005; Kirby and
52 Derakhti, 2019). These previous studies show that the spanwise (mostly alongshore) com-
53 ponent of vorticity is an important aspect of the breaking process. It is associated with
54 vertical shear generated by shallow breaking, which can produce traveling rolls through a
55 primary instability (Watanabe et al., 2005). The rolls, typical of unsteady parallel shear
56 flows, can subsequently evolve through a secondary instability to yield streamwise vorticity,
57 transitioning toward fully tridimensional turbulence. However, 2.5D CFD models are ap-
58 plied to individual breaking waves with only few alongshore wavelengths of the secondary
59 instability, precluding any evaluation of eddy statistics.

60 3D nonhydrostatic processes are usually studied independently of the two others (by
61 separate research communities) and rarely compared in terms of scales, magnitude and
62 interaction. The only attempt was made by Splinter and Slinn (2003) in a proceeding report.
63 Using a 3D nonhydrostatic model where breaking acceleration is introduced as a body force,
64 they show that deep breaking reproduces 2D model solutions, while the more realistic shallow
65 breaking process would hinder horizontal shear instability at the expense of vertical shear
66 instability. However, their domain size do not allow statistical comparisons and the profile of
67 breaking acceleration is imposed, not computed from a wave-resolving model. The present
68 study is a step forward from this early work, also addressing the case of short-crested wave
69 generation. Note that (Kumar and Feddersen, 2017) studied transient eddies produced by
70 a 3D nearshore circulation model, forced by short-crested waves computed beforehand with
71 a Boussinesq model. However, wave forcing is prescribed as a depth-uniform body force,
72 i.e., deep breaking, and could not produce vertical shear of the cross-shore flow. Their
73 hydrostatic assumption also precluded the model from vertical shear instabilities.

74 CROCO (Coastal and Regional Ocean Community model) is a new oceanic modeling
75 system built upon ROMS (Shchepetkin and McWilliams, 2005; Debreu et al., 2012), with
76 added non-Boussinesq kernel (Auclair et al., 2018). CROCO is designed for solving fine-scale

77 processes from the regional ocean to littoral zone with capabilities for LES in realistic config-
78 urations. Particular attention is given to numerical accuracy, high-performance computing
79 (optimization, scalability), portability and easy access (www.croco-ocean.org). This pa-
80 per presents a quick overview of the nonhydrostatic CROCO solver with a non-Boussinesq
81 (compressible) approach, before addressing its application to nearshore dynamics. First,
82 its ability to simulate surface gravity wave propagation and nearshore breaking is validated
83 against laboratory experiment. Second, we analyse and validate a full 3D, wave-resolving,
84 real-case simulation of transient rips, in the presence (or not) of short-crested waves and
85 strong alongshore currents. We discuss fundamental differences in the generation of surf
86 eddies by 3D wave-resolving models compared with depth-averaged models, with a focus on
87 the vertical structure of currents produced by shallow breaking and associated turbulence.
88 We conclude on the limitation of simplified vorticity evolution equations in which only the
89 vertical part is considered when so much activity lies in horizontal vorticity, governed by 3D
90 nonhydrostatic equations.

91 **2. Model description**

92 Because of limited computational resources, 3D wave-resolving models are still rarely
93 used in realistic study of surfzone dynamics. LES applications appeared in the 1990s and
94 are generally restricted to 2.5D laboratory-scale experiments of individual wave breaking.
95 Early applications used the volume-of-fluid (VOF) method for free-surface tracking (e.g., Lin
96 and Liu 1998; Watanabe and Saeki 1999; Watanabe et al. 2005; Derakhti and Kirby 2014).
97 This model type with Cartesian coordinate, where the free surface crosses computational
98 cells arbitrarily, fails to precisely apply the pressure boundary condition on the free surface,
99 affecting the model accuracy.

100 More recently, several 3D wave-resolving, free-surface and terrain-following models have
101 emerged for the nearshore zone, e.g., SWASH (Zijlema et al., 2011) and NHWAVE (Ma
102 et al., 2012; Derakhti et al., 2016), based on earlier attempts (e.g., Lin and Li 2002). In this
103 case, explicit free-surface overturning, occurring during breaking, is precluded and must be
104 parametrized as a turbulent or a shock process. However, these models can be accurate as

105 well as computational efficient in the study of waves and wave-driven mean and transient
106 circulation.

107 CROCO belongs to this class of models but, unlike other attempts, resolves the full
108 compressible Navier-Stokes equations (Auclair et al., 2018). A compressible approach pre-
109 serves the hyperbolic nature of Navier-Stokes equations and does not require a global elliptic
110 solver with incremental pressure corrections to ensure the incompressible mass balance. As
111 a result, it avoids splitting errors between pressure and velocity and approximations made
112 on free-surface conditions (Zijlema et al., 2011), thereby preserving amplitude and disper-
113 sion properties of nonhydrostatic surface waves. In the same time, the absence of global
114 computations by an elliptic solver makes parallelization and optimization procedures much
115 more efficient. The cost of solving acoustic waves is managed with a splitting technique
116 introduced below.

117 *2.1. Free-surface, compressible ocean model equations*

118 The full set of Navier-Stokes equations for a free-surface ocean is explicitly integrated in
119 the nonhydrostatic, non-Boussinesq (compressible) version of CROCO, built upon the code
120 structure of the Regional Oceanic Modeling System (ROMS) primitive equations (Shchep-
121 etkin and McWilliams, 2005). In the compressible approach (Auclair et al., 2018), acoustic
122 waves are solved explicitly to avoid Boussinesq degeneracy, which inevitably leads to a 3D
123 Poisson system in nonhydrostatic incompressible methods – detrimental to computational
124 costs and accuracy of free-surface model implementation.

125 An advantage of a nearshore model built on a general circulation model, originally de-
126 signed for larger scales ($\sim 100\text{m}-100\text{km}$), is to bridge ocean sciences (and their communities)
127 and reach otherwise unattainable objectives, such as addressing surf-shelf interactions in
128 a rotating and stratified framework. It also gives access to capabilities long developed in
129 oceanic models (high performance computing; high-order numerical schemes; coupling with
130 biogeochemistry and sediment models). The wave-resolving version of the model can also be
131 directly compared with wave-averaged equations, also implemented in ROMS and CROCO
132 (Marchesiello et al., 2015; Uchiyama et al., 2010), which rely more heavily on parametriza-

133 tions.

134 Non-Boussinesq equations include the momentum and continuity equations, the surface
 135 kinematic relation (for free surface), heat, salt or other tracer C conservation equations, and
 136 the equation of state, which reads in Cartesian coordinates:

$$\frac{\partial \rho u}{\partial t} = -\vec{\nabla} \cdot (\rho \vec{v} u) + \rho f v - \rho \tilde{f} w - \frac{\partial P}{\partial x} + \mathcal{F}_u + \mathcal{D}_u + \lambda \frac{\partial \vec{\nabla} \cdot \vec{v}}{\partial x} \quad (1)$$

$$\frac{\partial \rho v}{\partial t} = -\vec{\nabla} \cdot (\rho \vec{v} v) - \rho f u - \frac{\partial P}{\partial y} + \mathcal{F}_v + \mathcal{D}_v + \lambda \frac{\partial \vec{\nabla} \cdot \vec{v}}{\partial y} \quad (2)$$

$$\frac{\partial \rho w}{\partial t} = -\vec{\nabla} \cdot (\rho \vec{v} w) + \rho \tilde{f} u - \frac{\partial P}{\partial z} - \rho g + \mathcal{F}_w + \mathcal{D}_w + \lambda \frac{\partial (\vec{\nabla} \cdot \vec{v})}{\partial z} \quad (3)$$

$$\frac{\partial \rho}{\partial t} = -\vec{\nabla} \cdot (\rho \vec{v}) \quad (4)$$

$$\frac{\partial \eta}{\partial t} = w_f|_{z=\eta} - \vec{v}|_{z=\eta} \cdot \vec{\nabla} \eta \quad (5)$$

$$\frac{\partial \rho C}{\partial t} = -\vec{\nabla} \cdot (\rho \vec{v} C) + \mathcal{F}_C + \mathcal{D}_C \quad (6)$$

137 (u, v, w) are the (x, y, z) components of vector velocity \vec{v} ; η is the free surface; $\phi(x, y, z, t)$
 138 is dynamic pressure $\phi = P/\rho_0$, with P the total pressure; $\rho_0 + \rho(x, y, z, t)$ is total *in situ*
 139 density; $f(x, y)$ and $\tilde{f}(x, y)$ are the traditional and non-traditional Coriolis parameters,
 140 function of latitude; g is acceleration of gravity; $\mathcal{D}_u, \mathcal{D}_v, \mathcal{D}_C$ are diffusive terms; $\mathcal{F}_u, \mathcal{F}_v, \mathcal{F}_C$
 141 are forcing terms; λ is the second (bulk) viscosity, associated with compressibility (used to
 142 damp acoustic waves).

143 2.2. Time-splitting principle

144 In the above set of equations, a relation between ρ and P is required. To that end, and
 145 as part of a time-splitting approach, density is decomposed into slow and fast components

146 based on a first-order decomposition with respect to total pressure. In the following, s and
 147 f subscripts refer to slow and fast-mode components respectively:

$$\rho = \rho_s(T, S, P_s) + \overbrace{\frac{\partial \rho}{\partial P} \Big|_{T,S} \delta P + O(\delta P^2)}^{\rho_f = c_s^{-2} P_f} \quad (7)$$

$$P = \underbrace{P_{atm} + \int_z^\eta (\rho_s - \rho_0) g \, dz'}_{SLOW} + \underbrace{\rho_0 g (\eta - z) + \overbrace{\delta P}^{P_f}}_{FAST} \quad (8)$$

148 c_s is the speed of sound and $\delta P = P_f$ is the nonhydrostatic pressure.

149 The Navier-Stokes equations are then integrated with two different time steps within
 150 the time-splitting approach inherited from ROMS. The slow-mode integration is similar to
 151 ROMS with the addition of the slow part of vertical momentum equation, whereas fast-
 152 mode integration is 3D and includes the compressible terms of momentum and continuity
 153 equations. In vector form:

$$\begin{aligned} \frac{\partial \rho \vec{v}}{\partial t} = & \underbrace{-\vec{\nabla} \cdot (\rho \vec{v} \otimes \vec{v}) - 2\rho \vec{\Omega} \times \vec{v} - \vec{\nabla} \left(\int_z^{\eta_f} (\rho_s - \rho_0) g \, dz' \right) + \vec{\mathcal{F}}_{\vec{v}} + \vec{\mathcal{D}}_{\vec{v}}}_{SLOW} \\ & \underbrace{-\rho_0 g \vec{\nabla} \eta_f - \vec{\nabla} P_f + \rho \vec{g} + \lambda \vec{\nabla} (\vec{\nabla} \cdot \vec{v})}_{FAST} \end{aligned} \quad (9)$$

$$\frac{\partial \rho_f}{\partial t} = -\frac{\partial \rho_s}{\partial t} - \vec{\nabla} \cdot (\rho \vec{v}) \quad (10)$$

$$P_f = c_s^2 \rho_f \quad (11)$$

$$\frac{\partial \eta_f}{\partial t} = w_f|_{z=\eta} - \vec{v}_f|_{z=\eta} \cdot \vec{\nabla} \eta_f \quad (12)$$

$$\frac{\partial \rho C_s}{\partial t} = -\vec{\nabla} \cdot (\rho \vec{v} C_s) + \mathcal{F}_C + \mathcal{D}_C \quad (13)$$

$$\rho_s = \rho(T_s, S_s, \eta_f) \quad (14)$$

$$\rho = \rho_s + \rho_f \quad (15)$$

154 The momentum is integrated both in slow and fast modes but the right-hand-side of
 155 the equation is split in two parts: a slow part, made of slowly varying terms (advection,
 156 Coriolis force, baroclinic pressure force and viscous dissipation), and a fast part, made of fast-
 157 varying terms (the surface-induced and compressible pressure force, weight, and dissipation
 158 associated with bulk-viscosity). This momentum equation is numerically integrated twice,
 159 once with a large time-step keeping the fast part constant, and once with a smaller time-step
 160 keeping the slow part constant. This is much more computationally efficient than integrating
 161 the whole set of equations at the same fast time step. More details can be found in Auclair
 162 et al. (2018)¹. Note that acoustic waves can become pseudo-acoustic if their phase speed
 163 c_s is artificially reduced (c_s is a model parameter). In this case, high-frequency processes
 164 associated with bulk compressibility may be unphysical, but an accurate solution for slower
 165 nonhydrostatic dynamics can be preserved, while relaxing CFL constraints.

166 2.3. Discretized equations for nearshore application

167 In this study, motions are produced by an offshore wave-maker in a non-rotating, ho-
 168 mogeneous fluid. In this case, the Coriolis force, baroclinic pressure force and all surface
 169 fluxes are null. There is no temperature and salinity stratification so that slow density ρ_s is
 170 constant in time and space.

171 CROCO is discretized on a C-grid with finite-difference methods for slow and fast
 172 modes that are detailed elsewhere (Shchepetkin and McWilliams, 2005; Soufflet et al., 2016).

¹Auclair et al. (2018) presents a first implementation of the compressible approach involving a 3-level time splitting (internal, external and acoustic). CROCO was simplified to only retain a slow and a fast time level, where acoustic waves are solved together with the external (depth-averaged) mode. This procedure is more computationally efficient

173 In short, the slow-mode time-stepping algorithm is a Leapfrog Adams-Moulton predictor-
 174 corrector scheme, that is third-order accurate for the integration of advective terms. The
 175 fast mode is integrated with a generalized forward-backward scheme, which is also third-
 176 order accurate. Vertical flux terms that do not require accuracy (vertical diffusion term in
 177 the slow mode and all acoustic terms of w equation in the fast mode) are computed with an
 178 implicit time stepping to increase computational stability.

179 Horizontal and vertical advection terms are discretized using the WENO5-Z improved
 180 version of the 5th-order weighted essentially non-oscillatory scheme (Borges et al., 2008),
 181 which is popular for hyperbolic problems containing both shocks and smooth structures.
 182 WENO5-Z naturally takes care of dispersive numerical modes as well as shocks caused by
 183 breaking waves. Additionally, a 3D Smagorinsky model is used for turbulent closure on
 184 anisotropic grids:

$$\nu_t = (C_S \Delta)^2 |S| \quad (16)$$

185 where S is the 3D strain rate, Δ the grid-characteristic length scale ($\sqrt{d_x d_y}$ for horizontal
 186 viscosity and d_z for vertical viscosity), and C_S the Smagorinsky coefficient. The standard
 187 value of $C_S = 0.1$ (Canuto and Cheng, 1997) is used and sensitivity to this value is discussed
 188 along the paper.

189 2.4. Wave maker at offshore boundary

190 The wave maker forces a spectrum of 3D linear waves at the offshore boundary, as in
 191 Zijlema et al. (2011), rather than as an interior source term (Wei et al., 1999). The spectrum
 192 has frequency and directional spreading similar to Feddersen et al. (2011):

$$\eta_{bc}(y, t) = \sum_i a_i \sum_j d_j \cos(k_{y,ij} y - \omega_i t - \phi_{ij}) \quad (17)$$

193

$$\text{with } d_j = \exp\left(-\frac{\theta_j - \theta_m}{\sigma_\theta^2}\right) \text{ and } \sum d_j = 1 \quad (18)$$

194

$$u_{bc}(y, t) = \eta_{bc}(y, t) \omega_p \cos(\theta_m) \frac{\cosh(k_p(z+h))}{\sinh(k_p h)} \quad (19)$$

195

$$v_{bc}(y, t) = \eta_{bc}(y, t) \omega_p \sin(\theta_m) \frac{\cosh(k_p(z + h))}{\sinh(k_p h)} \quad (20)$$

196 where (i, j) are indices of spectral distribution in frequency and direction respectively; a_i is
 197 the amplitude at each frequency ω_i ; $k_{y,ij} = k_i \sin(\theta_j)$ is the alongshore wavenumber, where
 198 k_i is the linear theory wavenumber: $\omega_i^2 = g k_i \tanh(k_i h)$, and θ_j is wave angle; θ_m is the
 199 mean wave direction and σ_θ the directional spread around the mean; ω_p and k_p are peak
 200 frequency and wavenumber; d_j is a normalized frequency-dependent directional distribution;
 201 ϕ_{ij} is a uniformly distributed random phase.

202 Here w_{bc} is set to zero and our tests show only weak sensitivity to this choice. Depth-
 203 averaged (barotropic) velocities (\bar{u}, \bar{v}) must be provided as well in the wave maker because
 204 they are prognostic variables of our split-explicit model, advanced together with the fast
 205 acoustic mode. For normal depth-averaged velocity \bar{u} , we do not impose the depth-averaged
 206 value of u_{bc} directly but the value of the incoming characteristic of the shallow water system
 207 as in Flather-type conditions (Marchesiello et al., 2001; Blayo and Debreu, 2005):

$$\bar{u} = \bar{u}_{bc} - \sqrt{\frac{g}{h}} (\eta - \eta_{bc}) \quad (21)$$

208 This allows infragravity waves generated inside the domain to propagate out as long waves,
 209 while ensuring a near conservation of mass and energy through the open boundary.

210 3. Validation in Flume experiment

211 3.1. GLOBEX experiment

212 As a first step towards 3D modeling, we present here a validation of wave propagation
 213 and breaking using a wave flume experiment. The Gently sLOping Beach EXperiments
 214 (GLOBEX) were performed in the Scheldt flume of Deltares (Delft, the Netherlands) in
 215 2012, and described in Michallet et al. (2014). The project objective was to collect high-
 216 resolution space-time data of the cross-shore evolution of short and infragravity waves on a
 217 gentle slope for a range of wave conditions.

218 The flume is 110 m long, 1 m wide and 1.2 m high. The waves were generated with a
219 piston-type wave maker equipped with Active Reflection Compensation to minimize reflec-
220 tions from the wave paddle. A concrete beach with a 1:80 slope was constructed, with its
221 toe at 16.57 m from the wave maker. All experiments were run with a still water depth of
222 0.85 m and still-water shoreline at $x = 84.57$ m. The material that was laying loose on the
223 concrete bed before the flume was filled with water had a median grain size $D_{50}=0.75$ mm
224 (roughness length $z_0 \sim D_{50}/12 = 0.0625$ mm).

225 Sea-surface elevation measurements were taken at 190 locations (repeating a experiment
226 ten times while relocating the 21 wave gauges), together with velocity measurements at
227 43 locations, mostly (but not always) at 1 cm above bed to focus on the undertow. The
228 sampling frequency of the instruments during these experiments is 128 Hz. We will com-
229 pare experiment B3 corresponding to second-order (Stokes) wave generation of bichromatic
230 frequencies. The characteristics are as follows: $a_1 = 0.09$ m; $a_2 = 0.01$ m; $f_1 = 0.420$
231 Hz; $f_2 = 0.462$ Hz (short-wave peak period $T_p = 2/(f_1 + f_2) = 2.27$ s; and group period
232 $T_g = 1/(f_2 - f_1) = 23.81$ s). The signal had a total duration of 75 minutes.

233 3.2. Model comparison

234 The model is set-up with the same conditions as the wave flume experiment. Second-
235 order bichromatic waves are generated at the offshore boundary, with shore normal direction
236 and zero directional spread.

237 Figure 1 compares an Hovmuller plot (x,time) of data and model sea level η and undertow
238 u_b . When data is missing in the measurements, it is also removed from the model output.
239 The general structure reflecting wave speed and frequencies, wave packets, surf and swash
240 zones are all very similar. Some scattering in the data is particularly noticeable in the mean
241 undertown. As explained by Michallet et al. (2014), it may be attributed to the presence of
242 secondary motions generated by transverse waves at the break point where the transverse
243 mode-1 seiche can be excited at frequency $f_1 + f_2$.

244 A snapshot of wave field across the flume during runup condition is presented in Figure
245 2. It highlights the main processes of propagation, nonlinear interaction, shoaling, breaking,

246 roller propagation and runup. Non-linearity is apparent in both model and data in the
247 increasingly non-sinusoidal shape of short waves as they approach the shore (Elgar and
248 Guza, 1985).

249 Wave statistics are shown in Figure 3: standard deviation (or H_s), mean, skewness and
250 kurtosis. The envelop of all statistics are well reproduced by the model. Details of skewness
251 and kurtosis may differ due to irregular current measurement depth and transverse modes
252 in surfzone measurement. Despite scattering in the mean offshore-directed undertown data,
253 the model appears to reproduce the cross-shore undertow profile. In doing so, it obviously
254 outperforms depth-averaged Boussinesq models (Michallet et al., 2014). The undertow is
255 part of a vertical recirculation associated with breaking-induced surface onshore flow. Here,
256 we call undertow the bottom return flow (10 cm/s in this experiment). There is also an
257 Eulerian compensation flow for the onshore surface Stokes drift (continuity of total flow
258 must be preserved), which is sometimes referred to as undertow. This compensation flow is
259 the only cross-shore flow captured by depth-averaged models and is relatively weak (on the
260 order of 1 cm/s in this simulation).

261 From sensitivity tests, it appears that a realistic reproduction of H_s cross-shore evolution
262 in the breaker zone ($x = 60 - 70$ m) is conditioned to using the shock capturing scheme
263 WENO5-Z. Using only Smagorinsky (or alternatively a $k - \epsilon$ model) would fail. This is in
264 line with the representation of wave breaking as bores or hydraulic jumps that should be
265 treated as a shock problem. On the other end, the WENO scheme is less efficient in the
266 roller zone ($x > 70$ m), where turbulent dissipation dominates over production (van der A
267 et al., 2017). There, the turbulent closure scheme takes over as main dissipation process (but
268 a Smagorinsky coefficient over 0.1 leads to overestimated dissipation in the breaker zone).
269 Therefore, our combination of numerical and physical closure with off-the-box parameters
270 provides a realistic framework for surfzone dynamics. The fact that no tuning was needed for
271 these schemes indicates that the model can be confidently applied to other configurations.

272 4. Real-scale beach experiment

273 We now turn to a full 3D experiment with longshore-uniform bathymetry. The configu-
274 ration is derived from Grand Popo Beach (6.2°N, 1.7°E, Benin, in the Gulf of Guinea; Fig.
275 4). This stretch of coast presents a longshore-uniform, low tide terrace and steep upper
276 shoreface (Almar et al., 2014, 2016) and a sandy wave-dominated and microtidal environ-
277 ment, exposed to S-SW long period swells generated at high latitudes in the South Atlantic
278 (Almar et al., 2015a). A field experiment was conducted at Grand Popo Beach from 10
279 to 18 March 2014 (Almar et al., 2014; Derian and Almar, 2017). For our setup, we focus
280 on conditions in the middle of the afternoon of March 13 2014. The weather, tides and
281 wave conditions were ideal: weak winds and wind waves well separated from a narrow-band
282 swell with significant wave height $H_s = 1.15$ m, peak period $Tp = 11$ s, and wave incidence
283 $D = 10^\circ$ from shore normal direction. The water was at mid neap tide level (low-tide ter-
284 race at about 1 m depth), promoting a narrow surfzone less than 50 m wide. A Nortek
285 high-frequency acoustic Doppler velocimeter (ADV) was deployed in the surfzone and a dye
286 release was conducted to monitor the dispersion induced by flash rips. This was coupled with
287 UAV flights (STB DS6 hexacopter) at an elevation of 100 m. The Drone camera (NIKON
288 D700) was looking down, with a vertical angle, and recorded 4256×2832 -px scenes at 1 Hz
289 (Almar et al., 2014; Derian and Almar, 2017).

290 4.1. Setup

291 The domain is 542 m alongshore by 240 m across-shore, with periodic alongshore bound-
292 ary conditions. In order to prevent distortion when oblique waves are used with periodic
293 conditions, the alongshore size is adjusted according to peak wavelength and mean wave
294 direction. This method proved to perform well even with long-crested waves. The grid
295 spacing is generally $dx = dy = 1$ m but one simulation is run with higher resolution of 0.5
296 m. There are 10 vertical levels regularly spaced between the free surface and bottom (a
297 simulation with 20 levels did not change the results much). The model time step is $dt =$
298 0.025 s (0.0125 s at 0.5 m resolution). The model bathymetry is longshore-uniform and built
299 with continuous functions to smoothly fit the low-tide terrace structure observed during the

300 survey of (Almar et al., 2014, 2018). Depth H is 8 m offshore to 1 cm at the shoreline, whose
301 position varies with swash oscillation, relying on a wetting-drying scheme (Warner et al.,
302 2013). Depth over the terrace is about 1 m according the afternoon mid-tide conditions of
303 March 13 2014.

304 The wave maker is set with following parameters: $H_s=1.15$ m, $Tp=11$ s, $D = 0^\circ$, 10°
305 or 20° ($D = 10^\circ$ for comparison with data in Sec 4.3), and directional spread $\sigma_\theta = 30^\circ$. A
306 JONSWAP spectrum is constructed with these parameters and a peak enhancement factor
307 γ of 3.3. The quasi-monotonic and shock-capturing WENO5-Z scheme is used again with
308 Smagorinsky turbulence closure and $C_S = 0.1$. Bottom roughness is $z_0 = 0.01$ mm, which
309 may seem low but gives a drag coefficient $C_D \sim 0.002$ in the surfzone ($C_D = \kappa^2/\ln(z_1/z_0)^2$,
310 with $\kappa = 0.41$ and $z_1 \sim H/10$ the first level height above bed), which is a usual value in
311 depth-averaged models (Chen et al., 2003; Feddersen et al., 2011). We follow the practice
312 of these models here to reproduce their results within the pseudo-2D approach described
313 below. It is of little consequence for 3D simulations because, as will be shown, they are
314 much less sensitive to bottom drag than 2D models (Sec. 5).

315 The model is run for an hour starting from rest and adjusting through a rapid spin-up
316 phase. Figure 5 shows a snapshot of sea level that shows realistic features: short-crested
317 waves generated at an angle refract and break, generating rollers, swash and some reflection.

318 CROCO comes with capabilities for water quality, marine ecosystem and sediment mod-
319 eling. In the present study, some of these capabilities are used with simple setup. First, we
320 introduce a passive tracer in the swash zone for comparison with dye releases made during
321 the beach survey. Second, a suspended sediment model (Blaas et al., 2007; Warner et al.,
322 2008) allows comparison of patterns with aerial photos taken during the survey and also
323 between simulations. We use a single fine sand class with settling velocity of 1 cm/s. For
324 resuspension, we consider only one layer of sediment for simplicity, then only two parameters
325 are needed: critical shear stress and erosion rate at the seafloor, expressed in the erosion

326 flux (Blaas et al., 2007):

$$E = E_0(1 - p) \left(\frac{\tau_b}{\tau_{cr}} - 1 \right) \quad \text{for } \tau_b > \tau_{cr}$$
$$E = 0 \quad \text{otherwise}$$

327 τ_b is the bottom shear stress computed by the model. E_0 is an empirical erosion rate set
328 to 10^{-5} kg/m²/s; p is the sediment porosity (0.41); τ_{cr} is the critical shear stress, i.e., the
329 threshold for initiation of sediment motion, set to 0.01 N/m².

330 4.2. Shallow vs. deep breaking (and a Boussinesq model)

331 The Peregrine vorticity generation process only requires short crested waves, with no
332 need for unstable longshore currents generated by oblique waves. Boussinesq models are very
333 efficient in this process, but an important question for us is whether a 3D model will remain
334 so. An essential difference between the two types of model is depth penetration of wave
335 breaking. In a 2D Boussinesq model, deep breaking is implicitly assumed as momentum is
336 transferred instantaneously to the depth-averaged flow. However, this is a crude assumption
337 as breaking-induced flow and turbulence is produced above trough level where the onshore
338 flow is located (Grasso et al., 2012; Derakhti et al., 2016; van der A et al., 2017). Splinter
339 and Slinn (2003) suggest that the deep breaking assumption of depth-averaged models is an
340 essential component of their dynamics. The results presented here are in agreement with
341 their study and we propose to assess the role of 3D dynamics on surf eddies by comparing
342 simulations forced by shallow and deep breaking. Deep breaking will constitute a pseudo-2D
343 model whose results can be compared with a Boussinesq model solution (Section 4.5).

344 Boussinesq-type models (see Barthelemy 2004, for a review) are common tools to simulate
345 weakly dispersive waves and their transformations from the ocean to the swash zone. Several
346 developments allowed their application to a wide range of scales, from surfzone processes to
347 ocean basin-scale tsunami propagation (Kirby, 2016). Here, for a verification of our pseudo-
348 2D CROCO version, we use FUNWAVE-TVD (Shi et al., 2012). It solves the fully nonlinear
349 Boussinesq equations using a hybrid finite-volume finite-difference scheme. Parametrizations
350 are similar to CROCO, with wave breaking handled by a shock capturing TVD scheme

351 (making the need of explicit criterion unnecessary) and a quadratic drag formulation with
352 $Cd = 0.002$ for bottom friction.

353 To force deep breaking in a 3D wave-resolving model, we can artificially increase the
354 vertical turbulent viscosity around the breaker zone. Figure 6 shows a time and longshore
355 average of cross-shore and alongshore currents in the case of shallow and deep breaking.
356 Shallow breaking is computed by the 3D model with no explicit constrain on penetration
357 scale (but a parametrization of turbulence induced by breakers and currents). It drives a
358 shallow onshore flow about 40 cm deep and an offshore near-bottom undertow, resulting
359 in strong vertical shear of about 2 m/s within 1 m depth. With artificially strong vertical
360 viscosity, momentum in the breaker zone is almost instantly mixed to the bottom and the
361 cross-shore flow is reduced to nearly zero as required by mass-conservation (the residual
362 flow is the Stokes drift compensation flow), and consistent with depth-averaged models.
363 The longshore flow driven by oblique waves and a number of other simulations with shallow
364 and deep breaking (Tab. 2) will be analyzed and compared in the following sections.

365 *4.3. Reference simulations and comparison with data*

366 To introduce the 3D processes of flash rip generation, we present simulations with shal-
367 low and deep breaking (3D_SC_D10 and 2D_SC_D10), representing mid-tides conditions on
368 March 13 2014 in Grand Popo Beach. Figure 7 compares the vertical vorticity of surface
369 flow: $\omega_z = \frac{\partial v_s}{\partial x} - \frac{\partial u_s}{\partial y}$, averaged over two peak periods (22 s). With deep breaking (left
370 panel), the vortical field is rich with large filaments and surf eddies of 50-100 m scale that
371 are generated from short-crested waves, similar to Boussinesq model solutions. However,
372 the full 3D model with shallow breaking offers a radically new solution (Fig. 7, right panel).
373 Some of the large-scale fluctuations are present but over-shadowed by shorter scales. This
374 mode presents itself as rib structures (or mini rips following a relevant observation by Short
375 et al. 1993, already mentioned) with short longshore wavelength of order 5-10 m and periods
376 less than 5 min.

377 We now compare the two simulations with data collected during the survey of March
378 2014. Flash rips did not strike the survey team as particularly imposing (Castelle et al.,

379 2014; Scott et al., 2018; Floc’h et al., 2018). Dye experiments revealed filament generation,
380 but of relatively short scales. The survey was not extensive in terms of spatial resolution but
381 ADV and dye observations suggested a dynamical regime much closer to 3D shallow-breaking
382 than pseudo-2D deep-breaking simulations, as will be seen.

383 The dye experiment presented in Figure 8 illustrates both the structure of the alongshore
384 flow and scales of flash rips emerging from the surfzone. Using sequential photos of the tracer
385 from the Drone camera, it is possible to extract a simplified cross-shore profile of longshore
386 drift velocities (see Derian and Almar 2017 for more extensive Lagrangian calculations).
387 The result is presented in Figure 9 together with the model solutions with deep and shallow
388 breaking. The estimated longshore flow has an asymmetric V-shape very similar to the
389 full 3D model solution with a peak velocity of about 0.6 m/s in the inner surfzone. Deep
390 breaking solutions have a more symmetric profile centered in the outer surfzone. The profiles
391 in both simulations are a result of cross-shore advection. With deep breaking, advection is
392 weak and the longshore flow remains centered in the breaker zone (Fig. 6).

393 Some information on flash rips can also be extracted from the dye experiment. Figure 8
394 presents two consecutive aerial photos (at 154 s interval), and the corresponding snapshots
395 of tracer simulations with the full 3D model. We do not expect an exact match, considering
396 the chaotic nature of these phenomena, but scales and structures are meaningful. During
397 the survey, a few attempts of dye release were made before obtaining a clear filament patch.
398 Similarly for the model, we selected one occurrence among few tracer patches initialized
399 at regular interval along the coast (in the swash zone). Even though all tracer patches
400 eventually ended up with similar V-shape and similar scales of evolution, there was variability
401 in the evolution and we selected the most visually comparable filament with Drone photos.
402 In both cases, a thin filament of 5-10 m expands quickly seaward at a speed of 0.5-1 m/s,
403 reaching about 70 m from shore.

404 Another qualitative comparison of patterns can be made, looking at surfzone suspended
405 sediments in the aerial photo (Fig. 10, left panel). The contrasts in the photo is enhanced
406 to better expose suspended sediments (brown color), which is seen weakly extending beyond
407 the surfzone. Snapshots of the model’s surface sediment concentration is also shown after

408 15 min of simulation. With shallow breaking (center panel), sediments tend to resuspend
409 in the breaker zone and mix efficiently within the surf zone, but only weakly extend to the
410 innershelf. The rib structure is apparent at the seaward front of sediment concentration.
411 Overall, the patterns are very similar to the observed suspended sediments, particularly
412 evident in the upper part of the photo while the rest is partly masked by white foam or
413 sunglint. The same suspended sediment simulation with deep breaking gives very different
414 results (Fig. 10, right panel). Resuspension is now maximum in the inner surfzone (as for
415 eddy energy; Sec. 4.5). Filaments and eddies are more coherent, larger, their growth slower,
416 but they extend much further seaward. Mixing in the surfzone is less efficient than for the
417 shallow-breaking case, but shelf-surf exchange is more intense, due to filament extension.
418 This pattern may have better aesthetic values but does not fit visual observations of Grand
419 Popo Beach.

420 For a more quantitative scale comparison, we used ADV measurements, looking at hor-
421 izontal $u_h = \sqrt{u^2 + v^2}$ and vertical w velocities, the latter being a good indicator of 3D
422 motions. Figure 11 presents the Power Spectral Density (PSD) of u_h and w velocity fluctu-
423 ations for the model and the ADV data at a similar location in middle of the terrace. The
424 model short-wave spectrum around 11 s resulting from the wave maker is well represented
425 considering that the forced wave spectrum is constructed from JONSWAP approximation.
426 At lower frequency in both u_h and w PSD, a surprisingly good fit with data is given by the
427 full 3D model, while the deep-breaking simulation has a clear energy deficit. Looking at u
428 PSD, there is a band of high energy around 30-100s period that is clearly missing in the
429 pseudo-2D case. This frequency is consistent with visual inspection of rip structure oscilla-
430 tion in animated vorticity fields. However, the difference between 3D and pseudo-2D cases
431 can be seen at even lower frequency. This is best illustrated by w PSD and will be shown
432 to result from nonlinear upscaling (Sec. 4.6). Interestingly, the energy range of 3D eddies
433 encroaches on that of infragravity waves, making it hard to separate the two dynamics from
434 observations alone.

435 At an offshore position, where unfortunately no data is available, the comparison be-
436 tween model simulations shows a different relation at very low frequency, for time scales

437 between 3 and 15 min (Fig. 12). In this range, eddies produced by short-crested waves
 438 have more energy in the deep-breaking case, as expected from visual inspection of vorticity
 439 and suspended sediments. We conclude from this section that observations in Grand Popo
 440 Beach are in much better agreement with a full 3D solution of surf eddies, which presents
 441 a radically different dynamical regime. We will now analyze more closely the 3D structure
 442 and generation process of rib structures.

443 4.4. Structure and production of vertical shear instability

444 The surfzone eddy variability seen in the 3D model solution is truly three-dimensional.
 445 Vertical vorticity is only one manifestation, but horizontal vorticity is the key player. For
 446 better detection, we use a higher-resolution simulation (run for 15 minutes) that gives a
 447 very similar solution to the lower resolution case. Figure 13 presents the Q field defined
 448 by $Q = -\frac{1}{2} \frac{\partial u_i}{\partial x_j} \frac{\partial u_j}{\partial x_i}$, using Einstein summation convention over the three dimensions. Q
 449 is commonly used to enhance detection of vortical flows. Here, we split cross-shore and
 450 alongshore Q components ($Q_y = -\frac{\partial u}{\partial z} \frac{\partial w}{\partial x} - \frac{1}{2} \frac{\partial u^2}{\partial x}$ in red and $Q_x = -\frac{\partial v}{\partial z} \frac{\partial w}{\partial y} - \frac{1}{2} \frac{\partial v^2}{\partial y}$ in green),
 451 then normalize them and only plot positive isosurface values 0.02 for clarity (negative values
 452 give counter-rotating features).

453 The result is strikingly consistent with instabilities of a transitional mixing layer (Met-
 454 calfe et al., 1987; Lesieur, 1990), the transition being constrained by surfzone width. Q_y
 455 shows spanwise "rolls" created from the primary instability while Q_x identify streamwise
 456 "ribs" that are transverse (counter-rotating) vortices from secondary instability (assumably
 457 growing from perturbations generated between the rolls, in the braid region). Note that
 458 streamwise designate the shear direction, which is cross-shore rather than (oblique) wave
 459 direction. The reason is that the undertow aligns with surface flow in the alongshore di-
 460 rection, forming only weak mean longshore vertical shear. (Fig. 6). However, the rips can
 461 take an oblique direction as they are advected by the mean longshore flow. They extend
 462 seaward beyond the surfzone while stretching in the vertical direction. Filaments of verti-
 463 cal vorticity (or Q_z , not shown) also have similar rib structures to Q_x , recognisable in the
 464 surface vorticity plot of Figure 7.

465 The mean shear flow is composed of breaking-induced mean onshore flow and associated
466 seaward undertow (Fig. 6). The inflected velocity profile is inviscidly unstable to small per-
467 turbations and unstable modes of Kelvin-Helmholtz type can emerge. The spanwise rolls are
468 large vertical eddies that rapidly evolve into transverse (streamwise) rib vortices connected
469 by “braid” regions, and stretched seaward and downward. This picture is reminiscent of
470 descriptions based on laboratory-scale measurements and simulations (Nadaoka et al., 1989;
471 Watanabe et al., 2005; Kirby and Derakhti, 2019) — although here no air mixing by bubbles
472 is required for the secondary instability to occur.

473 According to linear stability analyses, the wavelength of primary shear instability setting
474 the distance between spanwise rolls is an order of magnitude larger than the mixing layer
475 width δ — in free shear layers (Michalke, 1964, 1965), wavelength, frequency and growth
476 rate of the most unstable modes are 14δ , $0.015 U/\delta$ and $0.1 U/\delta$ respectively). The sec-
477 ondary instability wavelength is of the same order as that of the primary instability ($2/3$
478 in Pierrehumbert and Widnall 1982). If the mixing layer width is taken as the vorticity
479 thickness $\delta = \Delta U / [\frac{\partial u}{\partial z}]_{max} \sim 60$ cm, then the wavelength of both roll and rib structures is
480 5-10 m, consistent with our simulation. Note that given an effective resolution of 5-10 dx for
481 CROCO (Soufflet et al., 2016), a simulation with 1-m grid resolution can only be considered
482 “eddy-permitting” for 3D instability in the present conditions. In terms of temporal modes,
483 the mixing layer size should produce modes of 0.01-0.04 Hz (25-100 s period), a range usually
484 reserved to surf beat. The model with 3D instability has energy in this range that is lacking
485 in the deep breaking case (see previous section and Fig. 11), but it has excess energy at
486 lower frequency as well, which results from upscaling through nonlinear interactions (the
487 same spectrum is produced with monochromatic wave forcing; see also Sec. 4.6).

488 In order to isolate the mechanism of eddy-mean flow interaction, we analyze a solution
489 forced with monochromatic, shore-normal, long-crested waves (3D_MONO_D0 in Tab. 2).
490 This simulation has constant wave forcing in both space and time when averaging over
491 the wave period (11 s). In this case, the same rib structure is generated (Fig. 14) but
492 without the large-scale alongshore variation seen in the full solution (Fig. 7, right panel).
493 A comparison of this simulation with other test cases will be presented in the next section.

494 Here, we analyse the mechanism and patterns of shear production. Figure 15 shows EKE
 495 source terms $-\overline{u'_i u'_j \frac{\partial \bar{u}_i}{\partial x_j}}$, that results from eddy-mean flow interaction, i.e., the energy spent
 496 by the mean flow to feed rolls and ribs. The largest term is vertical shear production
 497 $-\overline{u' w' \frac{\partial \bar{u}}{\partial z}}$ (Metcalf et al., 1987), with some lesser contribution from cross-shore convergence
 498 $-\overline{u' u' \frac{\partial \bar{u}}{\partial x}}$ (all other 7 combinations are negligible). The main production site is in the breaker
 499 zone. A maximum value is located just beneath the inflection point in the mean velocity
 500 profile (maximum shear represented in Fig. 15 by a thick blue line), consistent with mixing
 501 layer instability. The figure also presents a cross-section of mean 3D eddy kinetic energy
 502 ($EKE = \frac{1}{2}(u'^2 + v'^2 + w'^2)$, where u', v', w' are fluctuation velocities to the time-mean
 503 flow presented in Fig. 6). EKE and shear production have a very similar spatial pattern,
 504 although high EKE values extend from the production center in all directions: surface,
 505 bottom, shoreward and seaward. The primary rolls are thus produced in the outer surfzone
 506 and advected by the mean and eddy flow towards both the inner surfzone and innershelf.
 507 EKE transport is stronger at the surface, so that the streamwise filaments extend farther
 508 offshore at the surface than at the bottom (despite some amount of vertical stretching as
 509 they leave the terrace).

510 4.5. Short-crested waves and the Peregrine process

511 An important question of our study concerns the effect of wave variations (frequency and
 512 directional spreading) on flash rip generation in a full 3D model. To address this question, it
 513 is useful to simplify the problem and progressively add the multiple conditions of variability.
 514 In this section, we analyse shore-normal, short-crested wave simulations with shallow or deep
 515 breaking (3D_SC_D0 or 2D_SC_D0). Shore-normal conditions prevents the formation of a
 516 longshore current and associated horizontal shear instability. In addition, we look at long-
 517 crested wave solutions to isolate the effect of 3D instabilities, i.e., the monochromatic solution
 518 (3D_MONO_D0; presented in the previous section) and a similar case with JONSWAP
 519 frequency spectrum (3D_LC_D0). This latter comparison will help evaluate the effect of
 520 frequency spreading on eddy variability before addressing the effect of directional spreading.

521 Figure 16 compares vertical vorticity for shore-normal, short-crested wave cases. As for

522 oblique waves, deep-breaking leads to a rich vortical field with large filaments extending
523 far offshore, similarly to Boussinesq models. This is confirmed here with a comparison
524 between FUNWAVE-TVD and pseudo-2D CROCO applied to the same configuration. A
525 difference between Boussinesq and pseudo-2D solutions is the effect of 3D dynamics over the
526 innershelf in the latter case, where surface-intensified offshore eddies and filaments present a
527 more fragmented aspect due to forward energy cascade (Uchiyama et al., 2017; McWilliams
528 et al., 2018). However, the full 3D nonhydrostatic model with shallow breaking (Fig. 16,
529 right panel) shows patterns radically different from both Boussinesq and pseudo-2D solutions
530 with regular shorter-scale rib structures that present a more limited cross-shore extension.

531 Figure 17 presents EKE cross-sections for all shore-normal wave experiments. A striking
532 element of these figures is the presence of large surface and bottom EKE in the shallow
533 breaking cases. This pattern is not a result of shear production and is absent from the
534 monochromatic case (see previous section and Fig. 15). Therefore, it can only result from
535 wave groups associated with frequency spreading. Through wave height modulation, wave
536 groups produce variability in the breaking-induced surface onshore flow and associated un-
537 dertow. The variability amounts to about half of integrated mean EKE. However, it is much
538 reduced in the deep-breaking case, consistent with depth-averaged model studies (de Schip-
539 per et al., 2014).

540 We now turn to the effect of directional spreading. In Figure 17, short-crested waves
541 (produced by directional spreading) extend EKE production over a wider surf zone than long-
542 crested waves, where EKE is confined to the breaker zone. However, the seaward extension
543 is much larger in the pseudo-2D model, confirming the impression made from vorticity
544 inspection. Further confirmation is given by vertical EKE integration (and normalization
545 by mean depth; Fig. 18). It highlights 3 regions of eddy energy: the inner and outer
546 surfzone and innershelf. The top panel presents unfiltered data. In this case, 3D instability
547 and wave group forcing dominates eddy production in the outer surfzone. The most striking
548 observation is that the deep-breaking solution has a much larger cross-shore expansion,
549 stretching shoreward with a maximum in the inner surfzone and also 100 m seaward over
550 the innershelf.

551 Short-crested waves do not seem to affect 3D instability, while, on the contrary, shallow-
552 breaking largely affects eddy production associated with the Peregrine process. This is
553 particularly true for seaward extension. This is even clearer using a low-pass filter on velocity
554 fluctuations, removing a large part of variability from 3D instability and wave group forcing
555 (bottom panel of Fig. 18). What remains is closer to the usual definition of surfzone eddies
556 as Very Low Frequency features. They are much more energetic in the deep breaking case
557 (up to 3 times more than shallow breaking), showing a clearer EKE maximum in the inner
558 surfzone and a large patch over the innershelf. This result is consistent with the findings from
559 previous Boussinesq model studies that filaments forced by short-crested waves originate in
560 the inner surfzone, then spread offshore, forming eddies that grow in scale (Johnson and
561 Pattiaratchi, 2006).

562 *4.6. 2D and 3D surfzone turbulent cascade*

563 If there is energy produced by short-crested waves in the inner surfzone of the shallow
564 breaking case, the question is why does it not produced large filaments in the deep breaking
565 case. We found an answer in computing the spectrum energy flux. In 2D turbulence, the
566 flux of energy is negative and small fluctuations can grow into larger coherent structures.
567 This process is usually involved to explain the growth of filaments and eddies from variable
568 wave forcing (e.g., Johnson and Pattiaratchi 2006; Feddersen 2014).

569 To check its validity in a 3D model, we performed a wavenumber spectral flux analysis
570 for pseudo-2D and 3D simulations 2D_SC_D0 and 3D_SC_D0 (Fig. 19). The spectral flux
571 is computed as in Marchesiello et al. (2011) by spectral integration of v advection term.
572 Consistently with 2D turbulence there is a strong inverse cascade of kinetic energy (negative
573 flux) in the pseudo-2D model starting from the scale of injection corresponding to short-
574 crested wave forcing (wavelength of 30-40 m here), and there is no direct cascade towards
575 smaller scales. In the 3D case, the turbulent regime is very dissimilar. The negative flux of
576 energy produced by variable wave forcing is present but considerably reduced. In addition,
577 there is a second injection at smaller scales that corresponds to the most unstable mode of
578 3D instability (wavelength of 7-10 m). This small-scale energy travels both backward and

579 forward across the spectrum and thus widens the range of variability associated with 3D
580 instability. In the 3D long-crested wave case 3D_LC_D0, the same spectral flux is produced
581 at small scales but there is no large-scale inverse cascade due to missing injection by short-
582 crested waves.

583 This analysis shows that the growth of filaments and eddies associated with the Pere-
584 grine process heavily relies on a 2D inverse cascade that is not robust when extending to
585 3D dynamics. In this case, the vorticity fluctuation generated by variable waves cannot
586 transform into coherent structures as described for the 2D paradigm created by Boussinesq
587 models (Johnson and Pattiaratchi, 2006). The shallow water approximation simply does not
588 hold for nearshore wave-averaged currents.

589 *4.7. Oblique waves and horizontal shear instability*

590 The precedent experiments with shore-normal waves showed that shallow breaking tends
591 to hinder the generation of large 2D eddies by short-crested waves, while sustaining forced
592 and intrinsic 3D surfzone eddy dynamics. We now address the case of oblique waves by
593 increasing obliquity to $D = 20^\circ$ in order to generate longshore currents with larger horizontal
594 shear. From linear stability analysis of a 2D problem (Bowen and Holman, 1989), the
595 wavelength, frequency and growth rate of the most unstable shear waves are $\lambda_h = 2.5L$ and
596 $f_h = 0.07\frac{V}{L}$, $\sigma_h = 0.15\frac{V}{L}$ where V is the longshore current magnitude and L is the longshore
597 current half-width (outer shear). For a narrow, shoreline-intensified jet typical of Grand
598 Popo at mid-tide (Almar et al., 2014, 2015b), shear can be strong ($\sim 0.05 \text{ s}^{-1}$), implying a
599 minimum shear wave period of 5 min, wavelength of 80 m, and growth time $\sigma_h^{-1} = 3 \text{ min}$.

600 Forcing long-crested waves ($\sigma_\theta = 0$) with imposed deep breaking (2D_LC_D20), CROCO
601 recovers results that are typical of wave-averaged shallow-water models (or 3D models with
602 deep breaking as in Marchesiello et al. 2016, or Kumar and Feddersen 2017). Figure 20 (left
603 panel) shows an active horizontal shear instability producing shear waves with wavelength
604 consistent with linear theory. The shear waves propagate with the longshore current as
605 they become nonlinearly unstable, generating filaments and eddies that propagates offshore.
606 When both horizontal shear instability and short-crested wave vorticity generation are active

607 (with deep breaking), the result is even more energetic (Fig. 20, center panel). However,
608 with shallow breaking, the horizontal shear instability appears much weaker and is replaced
609 again by rib structures associated with vertical shear instability. Both processes appear
610 reduced by vertical shear.

611 Inspection of the cross-shore profile of mean longshore currents (Fig. 6) may help to
612 understand how shallow breaking undermine horizontal shear instability. With deep break-
613 ing, cross-shore advection is inactive and the longshore current remains trapped over the
614 terrace slope, and its outer shear is strong. With shallow breaking, however, the longshore
615 current is advected by the cross-shore recirculation, stretching its profile across the terrace
616 in a way that minimizes the outer shear. Then, the instability growth rate becomes too weak
617 to overcome friction (from turbulence or bottom drag). This may explain why Newberger
618 and Allen (2007) did not find horizontal shear instability in their 3D wave-averaged model
619 solutions as opposed to many previous 2D modeling studies (Allen et al., 1996; Slinn et al.,
620 1998; Uchiyama et al., 2009).

621 This process is verified in Figure 21, showing cross-sections of time-mean and longshore-
622 mean eddy and mean flow features for the four cases with oblique waves. Horizontal shear
623 instability is best assessed with the eddy-mean flow interaction term $-\overline{u'v'}\frac{\partial \bar{v}}{\partial x}$. In all cases,
624 shear production is clearly correlated with outer and inner slopes of the mean longshore
625 current, with stronger production in the outer shear. Deep-breaking cases show strong
626 shear production and large EKE patches centered over the terrace outer slope, where the
627 current shear is strongest. In the case of horizontal shear instability alone (2D_LC_D20), the
628 magnitude is lower than that of 2D_SC_D20, despite similar shear intensity. This indicates an
629 amplification of shear instability by short crested waves as they drive transient intensification
630 of longshore currents.

631 When comparing with shore-normal wave simulations of deep breaking cases, offshore
632 EKE seems nearly a linear combination of effects from short-crested waves and horizontal
633 shear instability. Offshore EKE extends further than predicted from shear production due to
634 mean and eddy advection, but short-crested waves clearly provide the most efficient process
635 for innershelf eddy activity.

636 The shallow-breaking cases (3D_LC_D20 and 3D_SC_D20) also features shear production,
637 but within a narrower zone and in shallower water, better controlled by friction. As a result,
638 EKE has a reduced amplitude. Short-crested waves (3D_SC_D20) appear to amplify the
639 inner surfzone energy (compared with 3D_LC_D20), but in both cases offshore energy is
640 weak. Over the innershelf, the EKE magnitude can be reduced by a factor 4-5.

641 5. Discussion and conclusion

642 Flash rips and surfzone eddies are traditionally conceived within a depth-averaged frame-
643 work that involves intrinsic horizontal shear instabilities or/and direct short-crested wave
644 vorticity generation. They are revisited in this study using a 3D nonhydrostatic wave-
645 resolving model applied to a real case with longshore-uniform topography at Grand Popo
646 Beach, Benin. We first presented a quick overview of a new free-surface, compressible ap-
647 proach adapted to wave-resolved nearshore dynamics. Its ability to simulate surface gravity
648 wave propagation and nearshore breaking is validated against laboratory experiment. Then,
649 the model is applied to Grand Popo Beach nearshore circulation generated by waves with
650 frequency and directional spreading. We assume based on comparison with Boussinesq solu-
651 tions that the essential difference between 2D and 3D models reduces to the vertical profile
652 of breaking acceleration, i.e., deep or shallow breaking. This allows a direct comparison of
653 2D and 3D frameworks within the same model equations and model setup.

654 The generation of transient rips by the 3D model is shown to differ considerably from
655 that produced by depth-averaged models, owing to the vertical structure of currents pro-
656 duced by shallow breaking. Processes of both horizontal shear instability and short-crested
657 wave breaking are restricted in a 3D model by the cross-shore vertical recirculation that
658 prevent a strong inverse cascade. Variable wave forcing (in space and time) tends to in-
659 crease flow variability in the surfzone (especially at the surface and bottom), but it does
660 not translate into large-scale rips streaming far offshore. Usual 2D mechanisms are replaced
661 by a Kelvin-Helmholtz-type instability, generating rib structures with spanwise and stream-
662 wise (alongshore and cross-shore) vorticity of intermediate scale between turbulence and
663 large horizontal eddies — periods of 30 s to a few minutes encroaching on the infragravity

664 wave range and wavelength around 5-10 m. Streamwise filaments extend beyond the sur-
665 fzone but with lower intensity than usual depth-averaged model rips (offshore mean EKE
666 is reduced by 50 percent). Energy spectra and visual inspections of tracer and sediment
667 concentration shows a much better fit of the 3D model patterns to observational data in
668 Grand Popo Beach. Our results thus question the qualitative and quantitative relevance of
669 depth-averaged models for nearshore dynamics.

670 These results are representative of mid-tide conditions of a low tide terrace with moderate
671 wave heights. Interestingly, the rib structures that are described here are comparable to the
672 *mini rips* described for similar conditions by Short et al. (1993): *Under typical mid-tide*
673 *conditions, with waves breaking across the bar, a low 'friendly' surf zone is produced. Waves*
674 *are less than 1 m and most water appears to head toward the shore. In fact it is return*
675 *seaward also, both by reflection of the beach face and via the mini rips, even if no rip*
676 *channel are present. The rips, however, are usually weak, ephemeral and shallow.*

677 In order to assess the ubiquity of mini rips in the nearshore zone, future 3D studies
678 should address different nearshore conditions. We assume that the result would be partic-
679 ularly sensitive to the penetration depth of wave breaking. As breaking-induced flow and
680 turbulence are mostly produced above trough level, the breaking vertical length-scale would
681 vary as the root-mean-square wave height H_{rms} (Uchiyama et al., 2010). In our model, it
682 is about half of H_{rms} . Therefore, in case of higher waves, higher penetration would reduce
683 vertical shear and increase the contribution of horizontal shear instability and short-crested
684 waves in surfzone eddy generation — as seen in overpublicized photos of large roll-up vortices
685 developing during high wave events. The penetration depth in our simulation is a function
686 of subgrid scale turbulence. Increasing the Smagorinsky coefficient from 0.1 to 0.5 (which
687 is an unrealistic limit, e.g., Canuto and Cheng 1997; Meyers and Sagaut 2006) reduces the
688 vertical shear and largely damps vertical shear instability — the frictional time h^2/ν_t is then
689 close to the growth time of about 1 minute. In this case, cross-shore advection is reduced and
690 the wave-averaged longshore flow remains in the breaker zone. Horizontal shear instability
691 is thus stronger, but the variability associated with short-crested waves, while increasing in
692 the inner surfzone, remains low on the innershelf. Therefore, even with high turbulence,

693 conventional 2D surf-shelf exchange processes are restrained.

694 Sensitivity to bottom roughness length z_0 is another interesting aspect of our tests. We
695 increased z_0 from 0.01 to 1 mm. In this case, the drag coefficient goes from about 0.002 to
696 0.008. Simulations with deep breaking were very sensitive to these values and the largest
697 roughness would completely shutdown horizontal shear instability due to shorter frictional
698 time (decreased from 5 to 2 min, i.e., shorter than growth time of about 5 min), and damp
699 short-crested wave vortical generation. On the contrary, full 3D solutions with shallow
700 breaking are weakly sensitive to bottom roughness, because of surface intensified currents
701 and shorter growth time of 3D instability. These tests inspire further confidence in our
702 results, while they point to an overemphasized importance given to bottom drag in studies
703 using depth-averaged models (e.g., Allen et al. 1996).

704 Finally, an important question is what exactly in the 3D model counteracts the generation
705 of surf eddies by short-crested waves. Vertical vorticity generation by the Peregrine process
706 can be written as:

$$\frac{\partial \omega_z}{\partial t} = - \frac{\partial F_{br}}{\partial y_c} \quad (22)$$

707 where F_{br} is the breaking force, extending to the bottom in a depth-averaged model, and y_c
708 is the along-crest direction. Using a breaking parametrization, Clark et al. (2012) propose
709 a scaling relation for vorticity generation of a single wave as $\frac{H_s^3}{h^{2.5}}$, at a maximum in the
710 outer surfzone. However, flash rip generation originates in the inner surfzone in depth-
711 averaged models (Johnson and Pattiaratchi, 2006) and in our deep breaking simulations. The
712 reason is that adding a transient source of vorticity is not enough to generate a horizontal
713 recirculation (with offshore filament). It needs a coastal boundary and an inverse energy
714 cascade that transform vorticity fluctuations into larger-scale coherent structures, as shown
715 by our spectral flux analysis (Sec. 4.6 and Fig. 19). In a 3D turbulent regime, this cascade
716 is much reduced (due to vortex tilting by the shear flow; McWilliams et al. 2018) and the
717 variability generated in the inner surfzone does not translate into large rips jetting offshore.
718 The inhibition of inverse cascade persist with higher viscosity ($C_s = 0.5$), which however
719 damps 3D instabilities. Therefore, tridimensionality is responsible for both counteracting

720 the generation of large horizontal eddies, and favoring that of intermediate-scale 3D mini
721 rips.

722 In conclusion, our results suggest that nearshore dynamics and transport processes may
723 be dominated by nonhydrostatic dynamics, not only for surface gravity waves as is known
724 since the 19th century, but also for vortical motions. This conclusion should hold for mod-
725 erate waves in other applications but further studies should explore the range of waves and
726 topographic conditions encountered in the global coastal ocean.

727 **Acknowledgement**

728 This research has received support from a consortium of French research agencies, as part
729 of CROCO's development project (GdR CROCO). It was granted access to the HPC re-
730 sources of CALMIP supercomputing center under allocation P19069. The fieldwork received
731 support by the French INSU/EC2CO program (Grand Popo Experiment). The data was ac-
732 quired by the authors and the CROCO source code is freely available at [www.croco-ocean.](http://www.croco-ocean.org)
733 [org](http://www.croco-ocean.org). Both observational and modeling data are available upon request.

734 **References**

- 735 van der A, D.A., van der Zanden, J., O'Donoghue, T., Hurther, D., Cáceres, I., McLelland, S.J., Ribberink,
736 J.S., 2017. Large-scale laboratory study of breaking wave hydrodynamics over a fixed bar. *Journal of*
737 *Geophysical Research: Oceans* 122, 3287–3310.
- 738 Akan, C., McWilliams, J.C., Uchiyama, Y., 2020. Topographic and coastline influences on surf eddies. *Ocean*
739 *Modelling* 147, 101565.
- 740 Allen, J.S., Newberger, P.A., Holman, R.A., 1996. Nonlinear shear instabilities of alongshore currents on
741 plane beaches. *Journal of Fluid Mechanics* 310, 181–213.
- 742 Almar, R., Almeida, P., Blenkinsopp, C., Catalan, P., 2016. Surf-swash interactions on a low-tide terraced
743 beach. *Journal of Coastal Research* 75, 348–352.
- 744 Almar, R., Du Penhoat, Y., Honkonnou, N., Castelle, B., Laibi, R., Anthony, E.J., Sénéchal, N., Degbe, G.,
745 Chuchla, R., Sohou, Z., Dorel, M., Mensah-Senoo, T., Quenum, M., Addo K., A., Ibaceta, R., Kestenare,
746 E., Zodehougan, G., Laryea W., S., Lefebvre, J., 2014. The Grand Popo experiment, Benin. *Journal of*
747 *Coastal Research SI* 70, pp. 651–656.

748 Almar, R., Kestenare, E., Reyns, J., Jouanno, J., Anthony, E., Laibi, R., Hemer, M., Du Penhoat, Y.,
749 R., R., 2015a. Response of the bight of benin (gulf of guinea, west africa) coastline to anthropogenic
750 and natural forcing, part1: Wave climate variability and impacts on the longshore sediment transport.
751 Continental Shelf Research 110, 48 – 59.

752 Almar, R., Larnier, S., Castelle, B., Scott, T., Floc’h, F., Detandt, G., 2015b. On the use of the radon
753 transform to estimate longshore currents from video imagery. Coastal Engineering 114, 301–308.

754 Almar, R., Lerma, A.N., Castelle, B., Scott, T., 2018. On the influence of reflection over a rhythmic swash
755 zone on surf zone dynamics. Ocean Dynamics , 1–11.

756 Ardhuin, F., Rasche, N., Belibassakis, K., 2008. Explicit wave-averaged primitive equations using a general-
757 ized lagrangian mean. Ocean Modelling 20, 35.

758 Auclair, F., Bordoio, L., Dossmann, Y., Duhaut, T., Paci, A., Ulses, C., Nguyen, C., 2018. A non-hydrostatic
759 non-boussinesq algorithm for free-surface ocean modelling. Ocean Modelling 132.

760 Barthelemy, E., 2004. Nonlinear shallow water theories for coastal waves. Surveys in Geophysics 25, 315–337.

761 Blaas, M., Dong, C., Marchesiello, P., McWilliams, J.C., Stolzenbach, K.D., 2007. Sediment-transport
762 modeling on southern californian shelves: A ROMS case study. Continental Shelf Research 27, 832 – 853.

763 Blayo, E., Debreu, L., 2005. Revisiting open boundary conditions from the point of view of characteristic
764 variables. Ocean Modelling .

765 Bonneton, P., Bruneau, N., Castelle, B., Marche, F., 2010. Large scale vorticity generation due to dissipating
766 waves in the surf zone. Discrete and Continuous Dynamical Systems - series B 13, 729–738.

767 Borges, R., Carmona, M., Costa, B., Don, W.S., 2008. An improved weighted essentially non-oscillatory
768 scheme for hyperbolic conservation laws. Journal of Computational Physics 227, 3191 – 3211.

769 Bowen, A.J., Holman, R.A., 1989. Shear instabilities of the mean longshore current: 1. theory. Journal of
770 Geophysical Research: Oceans 94, 18023–18030.

771 Canuto, V.M., Cheng, Y., 1997. Determination of the smagorinsky–lilly constant c_s . Physics of Fluids 9,
772 1368–1378.

773 Castelle, B., du Penhoat, Y., Almar, R., Anthony, E., Lefebvre, J.P., Laibi, R., Chuchla, R., Dorel, M.,
774 Senechal, N., 2014. Flash rip dynamics on a high-energy low-tide-terraced beach (grand popo, benin,
775 west africa). Journal of Coastal Research 70, 633–638.

776 Chen, Q., Kirby, J.T., Dalrymple, R.A., Shi, F., Thornton, E.B., 2003. Boussinesq modeling of longshore
777 currents. Journal of Geophysical Research: Oceans 108.

778 Clark, D.B., Elgar, S., Raubenheimer, B., 2012. Vorticity generation by short-crested wave breaking.
779 Geophysical Research Letters 39.

780 Cox, D.T., Anderson, S.L., 2001. Statistics of intermittent surf zone turbulence and observations of large
781 eddies using piv. Coastal Engineering Journal 43, 121–131.

782 Debreu, L., Marchesiello, P., Penven, P., Cambon, G., 2012. Two-way nesting in split-explicit ocean models:
783 Algorithms, implementation and validation. *Ocean Modelling* 49–50, 1 – 21.

784 Derakhti, M., Kirby, J.T., 2014. Bubble entrainment and liquid–bubble interaction under unsteady breaking
785 waves. *Journal of Fluid Mechanics* 761, 464–506.

786 Derakhti, M., Kirby, J.T., Shi, F., Ma, G., 2016. Nhwave: Consistent boundary conditions and turbulence
787 modeling. *Ocean Modelling* 106, 121 – 130.

788 Derian, P., Almar, R., 2017. Wavelet-based optical flow estimation of instant surface currents from shore-
789 based and uav videos. *IEEE Transactions on Geoscience and Remote Sensing* 55, 5790–5797.

790 Dodd, N., Iranzo, V., Reniers, A., 2000. Shear instabilities of wave-driven alongshore currents. *Reviews of*
791 *Geophysics* 38, 437–463.

792 Dodd, N., Oltman-Shay, J., Thornton, E.B., 1992. Shear instabilities in the longshore current: A comparison
793 of observation and theory. *Journal of Physical Oceanography* 22, 62–82.

794 Elgar, S., Guza, R.T., 1985. Observations of bispectra of shoaling surface gravity waves. *Journal of Fluid*
795 *Mechanics* 161, 425–448.

796 Feddersen, F., 2014. The generation of surfzone eddies in a strong alongshore current. *Journal of Physical*
797 *Oceanography* 44, 600–617.

798 Feddersen, F., Clark, D.B., Guza, R.T., 2011. Modeling surf zone tracer plumes: 2. transport and dispersion.
799 *Journal of Geophysical Research: Oceans* 116.

800 Floc’h, F., Mabiala, G., Almar, R., Castelle, B., Hall, N., Du Penhoat, Y., Scott, T., Delacourt, C., 2018.
801 Flash rip statistics from video images. *Journal of Coastal Research* 81, 100–106.

802 Grasso, F., Castelle, B., Ruessink, G., 2012. Turbulence dissipation under breaking waves and bores in a
803 natural surf zone. *Continental Shelf Research* 43, 133–141.

804 Henderson, S., Arnold, J., Özkan Haller, H., Solovitz, S., 2017. Depth dependence of nearshore currents and
805 eddies. *Journal of Geophysical Research: Oceans* 122.

806 Johnson, D., Pattiaratchi, C., 2006. Boussinesq modelling of transient rip currents. *Coastal Engineering* 53,
807 419 – 439.

808 Kirby, J.T., 2016. Boussinesq models and their application to coastal processes across a wide range of scales.
809 *Journal of Waterway, Port, Coastal, and Ocean Engineering* 142, 03116005.

810 Kirby, J.T., Derakhti, M., 2019. Short-crested wave breaking. *European Journal of Mechanics - B/Fluids*
811 73, 100–111.

812 Kumar, N., Feddersen, F., 2017. The effect of stokes drift and transient rip currents on the inner shelf. part
813 i: No stratification. *Journal of Physical Oceanography* 47, 227–241.

814 Kumar, N., Voulgaris, G., Warner, J.C., Olabarrieta, M., 2012. Implementation of the vortex force formalism
815 in the coupled ocean-atmosphere-wave-sediment transport (coawst) modeling system for inner shelf and

816 surf zone applications. *Ocean Modelling* 47, 65 – 95.

817 Lesieur, M., 1990. *Turbulence in Fluids. Fluid Mechanics and its Applications*, Springer Netherlands.

818 Lin, P., Li, C.W., 2002. A σ -coordinate three-dimensional numerical model for surface wave propagation.
819 *International Journal for Numerical Methods in Fluids* 38, 1045–1068.

820 Lin, P., Liu, P.L.F., 1998. A numerical study of breaking waves in the surf zone. *Journal of Fluid Mechanics*
821 359, 239–264.

822 Longo, S., Petti, M., Losada, I.J., 2002. Turbulence in the swash and surf zones: a review. *Coastal*
823 *Engineering* 45, 129 – 147. *Surface and Swash Zone Mechanics*.

824 Ma, G., Shi, F., Kirby, J.T., 2012. Shock-capturing non-hydrostatic model for fully dispersive surface wave
825 processes. *Ocean Modelling* 43-44, 22 – 35.

826 Marchesiello, P., Almar, R., Benshila, R., Larnier, S., Castelle, B., McWilliams, J.C., 2016. On eddy-mixed
827 longshore currents: Video observation and 3d modeling off grand popo beach, benin. *Journal of Coastal*
828 *Research* 75, 408–412.

829 Marchesiello, P., Benshila, R., Almar, R., Uchiyama, Y., McWilliams, J.C., Shchepetkin, A., 2015. On
830 tridimensional rip current modeling. *Ocean Modelling* 96, 36 – 48. *Waves and coastal, regional and global*
831 *processes*.

832 Marchesiello, P., Capet, X., Menkes, C., Kennan, S.C., 2011. Submesoscale dynamics in tropical instability
833 waves. *Ocean Modelling* 39, 31–46.

834 Marchesiello, P., McWilliams, J.C., Shchepetkin, A., 2001. Open boundary conditions for long-term inte-
835 gration of regional oceanic models. *Ocean modelling* 3, 1–20.

836 McWilliams, J.C., Akan, C., Uchiyama, Y., 2018. Robustness of nearshore vortices. *Journal of Fluid*
837 *Mechanics* 850, R2.

838 McWilliams, J.C., Restrepo, J.M., Lane, E.M., 2004. An asymptotic theory for the interaction of waves and
839 currents in coastal waters. *Journal of Fluid Mechanics* 511, 135–178.

840 Metcalfe, R.W., Orszag, S.A., Brachet, M.E., Menon, S., Riley, J.J., 1987. Secondary instability of a
841 temporally growing mixing layer. *Journal of Fluid Mechanics* 184, 207–243.

842 Meyers, J., Sagaut, P., 2006. On the model coefficients for the standard and the variational multi-scale
843 smagorinsky model. *Journal of Fluid Mechanics* 569, 287–319.

844 Michalke, A., 1964. On the inviscid instability of the hyperbolictangent velocity profile. *Journal of Fluid*
845 *Mechanics* 19, 543–556.

846 Michalke, A., 1965. On spatially growing disturbances in an inviscid shear layer. *Journal of Fluid Mechanics*
847 23, 521–544.

848 Michallet, H., Ruessink, B.G., Vieira Lima Matias da Rocha, M., De Bakker, A., Van Der A, D.A., Ruju,
849 A., Silva, P.A., Sénéchal, N., Mariou, V., Tissier, M., Almar, R., Abreu, T., Birrien, F., Vignal, L.,

850 Barthélemy, E., Mouazé, D., Cienfuegos, R., Wellens, P., 2014. GLOBEX: Wave dynamics on a shallow
851 sloping beach, in: HYDRALAB IV Joint User Meeting, Lisbon, July 2014, Lisbonne, Portugal.

852 Nadaoka, K., Hino, M., Koyano, Y., 1989. Structure of the turbulent flow field under breaking waves in the
853 surf zone. *Journal of Fluid Mechanics* 204, 359–387.

854 Newberger, P.A., Allen, J.S., 2007. Forcing a three-dimensional, hydrostatic, primitive-equation model for
855 application in the surf zone: 2. application to duck94. *Journal of Geophysical Research: Oceans* 112.

856 Özkan-Haller, H.T., Kirby, J.T., 1999. Nonlinear evolution of shear instabilities of the longshore current:
857 A comparison of observations and computations. *Journal of Geophysical Research: Oceans* 104, 25953–
858 25984.

859 Peregrine, D.H., 1998. Surf zone currents. *Theor. Comput. Fluid Dyn.* 10, 295–309.

860 Pierrehumbert, R., Widnall, S., 1982. The two- and three-dimensional instabilities of a spatially periodic
861 shear layer. *Journal of Fluid Mechanics* 114, 59 – 82.

862 de Schipper, M.A., Reniers, A.J., Ranasinghe, R., Stive, M.J., 2014. The influence of sea state on formation
863 speed of alongshore variability in surf zone sand bars. *Coastal Engineering* 91, 45 – 59.

864 Scott, T., Castelle, B., Almar, R., Senechal, N., Floc’h, F., D.G., 2018. Controls on flash rip current hazard
865 on low-tide terraced tropical beaches in west africa. *Journal of Coastal Research* 81, 92–99.

866 Shchepetkin, A.F., McWilliams, J.C., 2005. The regional oceanic modeling system (roms): a split-explicit,
867 free-surface, topography-following-coordinate oceanic model. *Ocean Modelling* 9, 347–404.

868 Shi, F., Kirby, J.T., Harris, J.C., Geiman, J.D., Grilli, S.T., 2012. A high-order adaptive time-stepping tvd
869 solver for boussinesq modeling of breaking waves and coastal inundation. *Ocean Modelling* 43-44, 36 –
870 51.

871 Short, A.D., Hogan, C.L., Safety, A.B., Program., M., 1993. Beaches of the New South Wales coast : a
872 guide to their nature, characteristics, surf and safety. Australian Beach Safety and Management Program
873 Beaconsfield, N.S.W.

874 Slinn, D.N., Allen, J.S., Newberger, P.A., Holman, R.A., 1998. Nonlinear shear instabilities of alongshore
875 currents over barred beaches. *Journal of Geophysical Research* 103, 18,357 – 18,379.

876 Soufflet, Y., Marchesiello, P., Lemarié, F., Jouanno, J., Capet, X., Debreu, L., Benshila, R., 2016. On
877 effective resolution in ocean models. *Ocean Modelling* 98, 36–50.

878 Splinter, K.D., Slinn, D.N., 2003. Three-dimensional modeling of alongshore current dynamics.

879 Svendsen, I.A., Madsen, P.A., 1984. A turbulent bore on a beach. *Journal of Fluid Mechanics* 148, 73–96.

880 Uchiyama, Y., McWilliams, J., Shchepetkin, A., 2010. Wave-current interaction in an oceanic circulation
881 model with a vortex-force formalism: Application to the surf zone. *Ocean Modelling* 34, 16–35.

882 Uchiyama, Y., McWilliams, J.C., Akan, C., 2017. Three-dimensional transient rip currents: Bathymetric
883 excitation of low-frequency intrinsic variability. *Journal of Geophysical Research: Oceans* 122, 5826–5849.

- 884 Uchiyama, Y., McWilliams, J.C., Restrepo, J.M., 2009. Wave-current interaction in nearshore shear insta-
885 bility analyzed with a vortex force formalism. *Journal of Geophysical Research: Oceans* 114.
- 886 Warner, J.C., Defne, Z., Haas, K., Arango, H.G., 2013. A wetting and drying scheme for ROMS. *Computers*
887 *and Geosciences* 58, 54 – 61.
- 888 Warner, J.C., Sherwood, C.R., Signell, R.P., Harris, C.K., Arango, H.G., 2008. Development of a three-
889 dimensional, regional, coupled wave, current, and sediment-transport model. *Computers & Geosciences*
890 34, 1284–1306.
- 891 Watanabe, Y., Saeki, H., 1999. Three-dimensional large eddy simulation of breaking waves. *Coastal Engi-*
892 *neering Journal* 41, 281–301.
- 893 Watanabe, Y., Saeki, H., Hosking, R.J., 2005. Three-dimensional vortex structures under breaking waves.
894 *Journal of Fluid Mechanics* 545, 291–328.
- 895 Wei, G., Kirby, J.T., Sinha, A., 1999. Generation of waves in boussinesq models using a source function
896 method. *Coastal Engineering* 36, 271 – 299.
- 897 Zijlema, M., Stelling, G., Smit, P., 2011. Swash: An operational public domain code for simulating wave
898 fields and rapidly varied flows in coastal waters. *Coastal Engineering* 58, 992 – 1012.

Table 1: Model setup of CROCO’s Grand Popo Beach configuration

Model parameters	Values
Grid type	Horizontal: rectangular, regular mesh; vertical: terrain following grid with free surface
Domain size (L_x, L_y)	240 x 542 m
Horizontal resolution (dx/dy)	1 m
Vertical grid (Nz)	10 levels (dz=10 cm over the terrace)
Time step	dt=0.025 s, dt _f =0.001 s, c _{sound} =200 m/s (pseudo-acoustic)
Bathymetry (h)	longshore-uniform low tide terrace derived from March 2014 survey
Tides	mid-tide: 1-m depth over the terrace
Wave forcing (u,v,w at offshore boundary)	linear wave solutions reconstructed from JONSWAP spectrum with $H_s = 1.15$ m and $T_p = 11$ s
Air-sea forcing (u,v,T,S fluxes)	0
Sediment model (D50, Ws, E_0 , τ_{cr})	$D50 = 100 \mu\text{m}$; $Ws=5$ mm/s; $E_0 = 10^{-5}$ kg/m ² /s; $\tau_{cr} = 0.01$ N/m ²
Breaking/turbulence	WENO5-Z shock-capturing advection scheme Smagorinsky SGS model ($C_S = 0.1$)
Bottom roughness (z_0)	0.01-1 mm

Table 2: List of CROCO simulations for Grand Popo Beach.

Simulation	Breaking	Wave type	Direction	Test
3D_SC_D10	shallow	short-crested	10°	Data vs. 3D instab. vs. Peregrine process
2D_SC_D10	deep	short-crested	10°	
3D_SC_D0	shallow	short-crested	0°	3D instab. vs. Peregrine process
2D_SC_D0	deep	short-crested	0°	
3D_LC_D0	shallow	long-crested	0°	
3D_MONO_D0	shallow	monochromatic	0°	
3D_SC_D20	shallow	short-crested	20°	3D instab. vs. 2DH instab. vs. Peregrine process
3D_LC_D20	shallow	long-crested	20°	
2D_SC_D20	deep	short-crested	20°	
2D_LC_D20	deep	long-crested	20°	
FUNWAVE-TVD	deep	short-crested	0°	Test of pseudo-2D CROCO

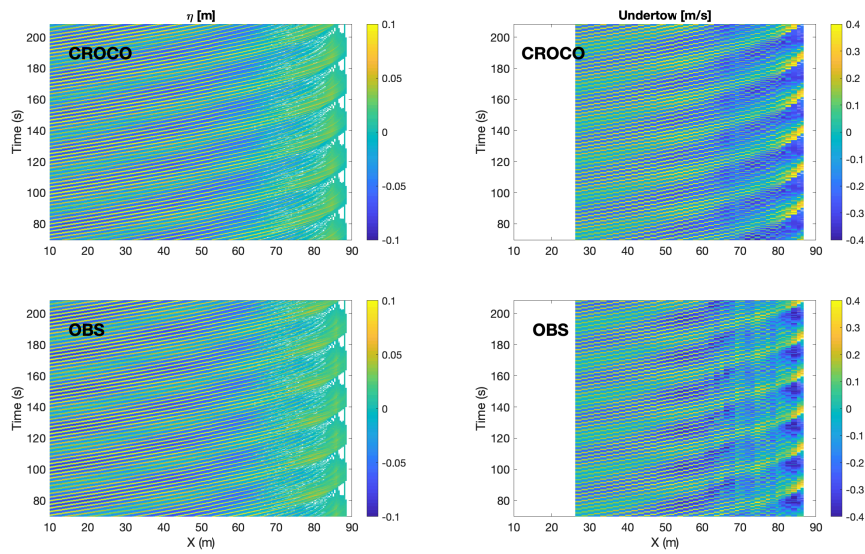


Figure 1: Hovmuller plot (x,time) of data and model sea level η and undertow u_b for the GLOBEX B3 flume experiment. When data is missing in the measurements, it is also removed from the model output.

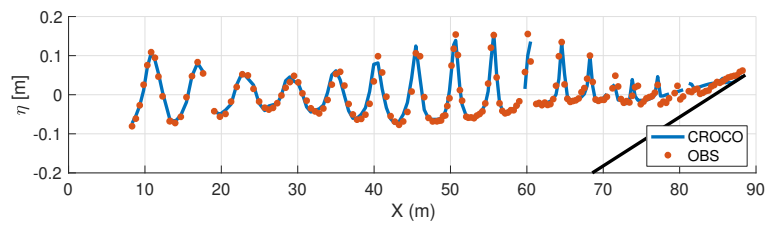


Figure 2: Snapshot of wave field across the GLOBEX B3 flume experiment during runup conditions for model (blue line) and data (red dots).

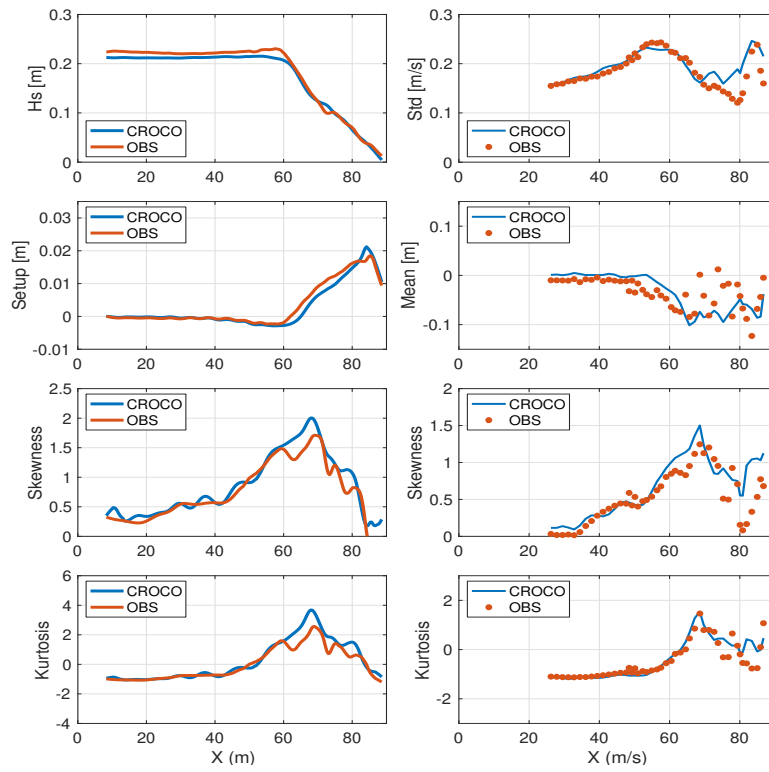


Figure 3: Wave statistics from GLOBEX B3 experiment for sea level η and undertow u_b in model (blue line) and data (red line or dots). From top to bottom: standard deviation (or H_s for η), mean, skewness and kurtosis.

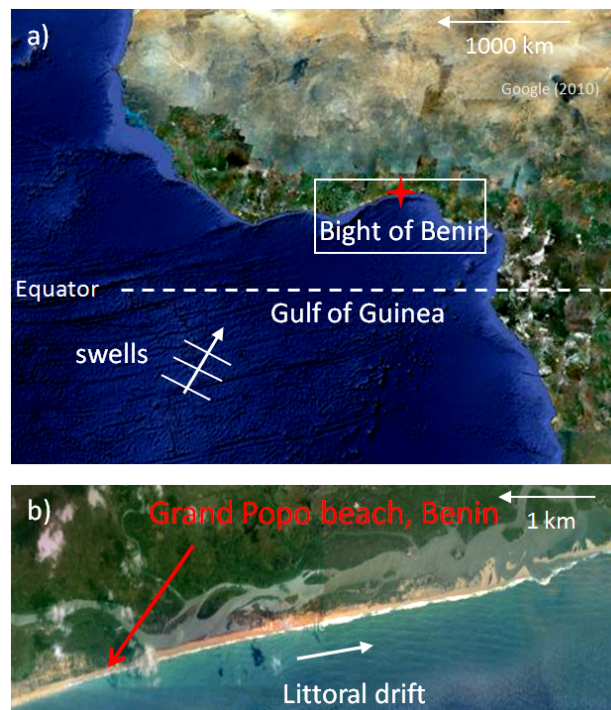


Figure 4: Grand Popo Beach, Benin, is a longshore uniform beach located in the Gulf of Guinea. It is representative of an open, wave-dominated and microtidal environment exposed to S-SW long period swells generated at high latitudes in the South Atlantic.

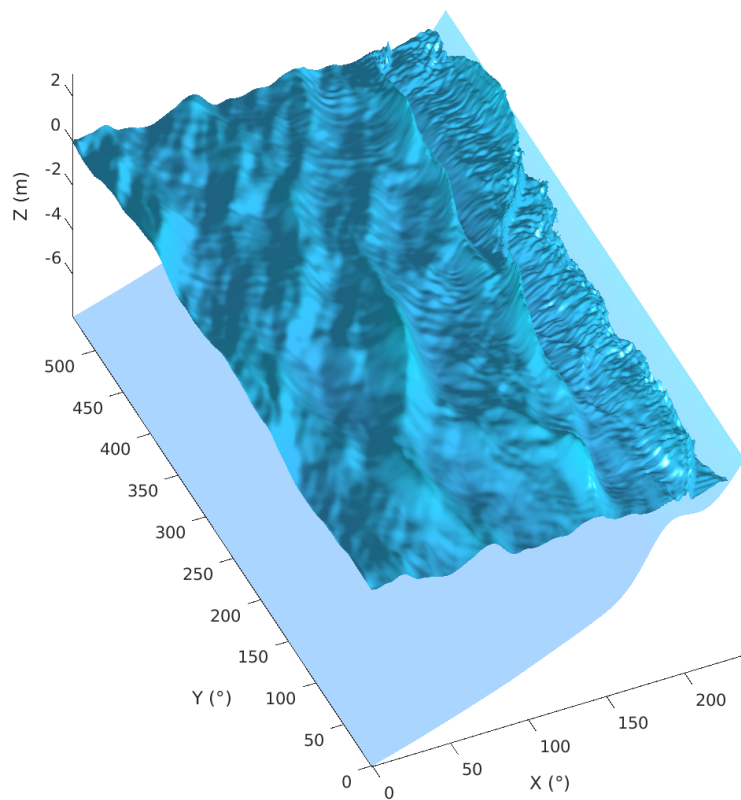


Figure 5: CROCO sea level snapshot, showing short-crested waves generated at the offshore boundary and propagating shoreward at an angle of 10° , with refraction and breaking through the surf and swash zones.

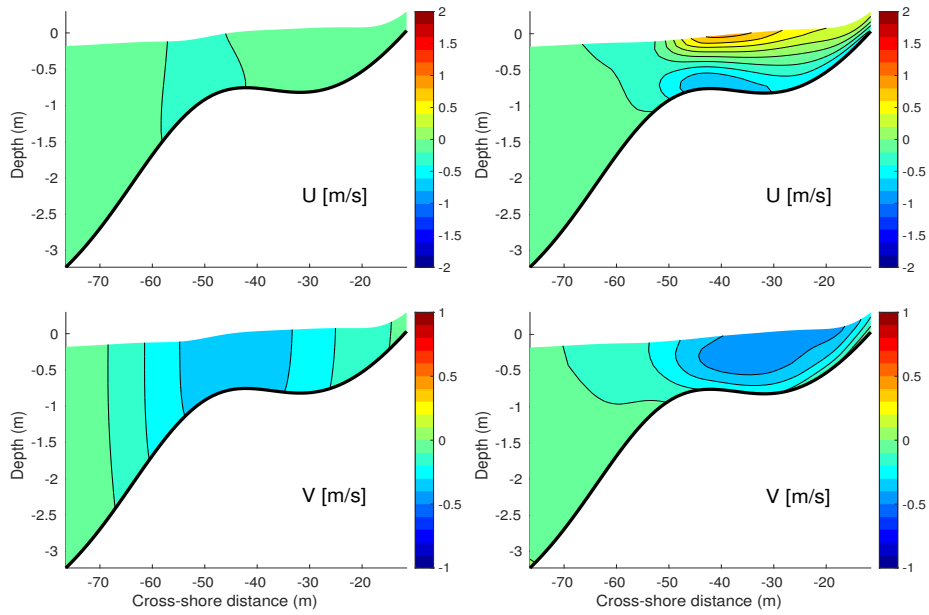


Figure 6: Cross-section of time-mean and longshore-mean, cross-shore (top) and longshore (bottom) currents in the case of shallow (right) and deep (left) breaking.

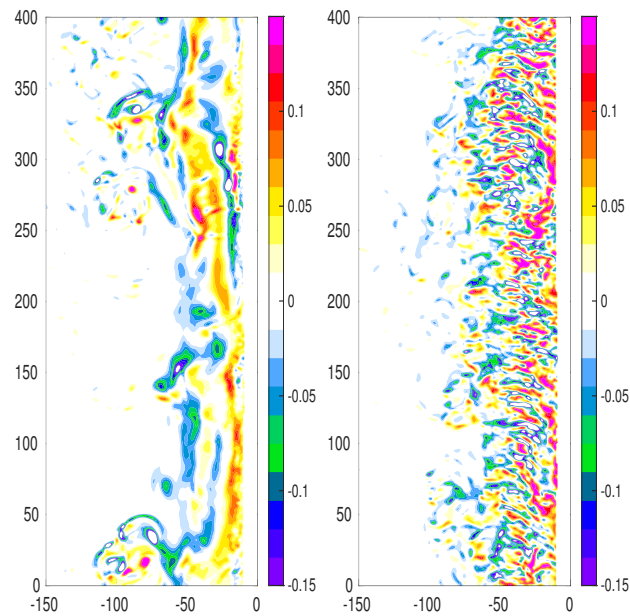


Figure 7: Vertical vorticity snapshot in the case of shallow (right) and deep (left) breaking.

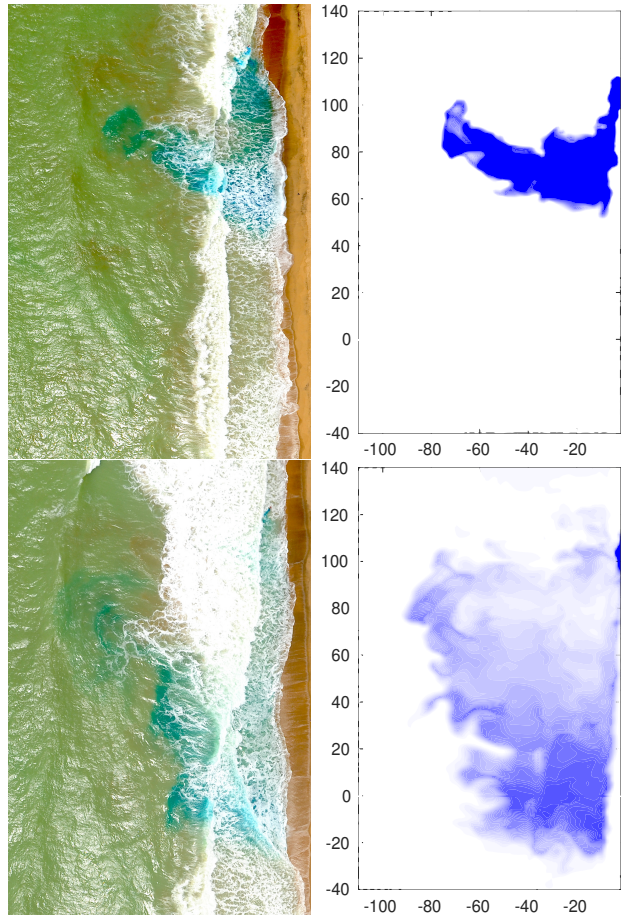


Figure 8: Drone photos (left) and CROCO simulations (right) of dye release at 154 s interval during the Grand Popo survey of March 13 2014 at afternoon mid-tide.

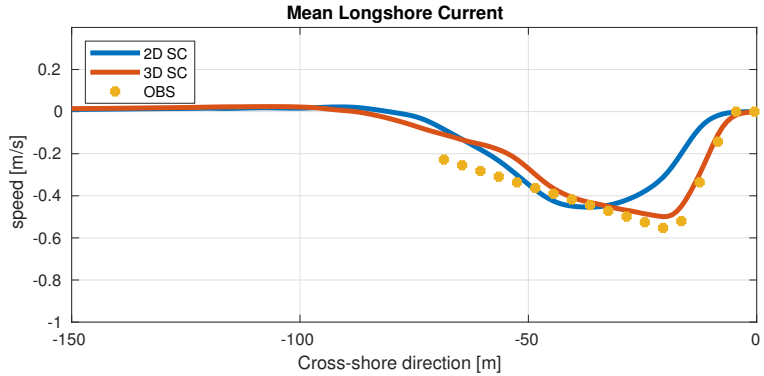


Figure 9: Cross-shore profile of time-mean and longshore-mean surface longshore flow for the full 3D simulation with wave direction $D = 10^\circ$. An estimation of Lagrangian velocities from drone photos of Figure 8 is added for comparison.

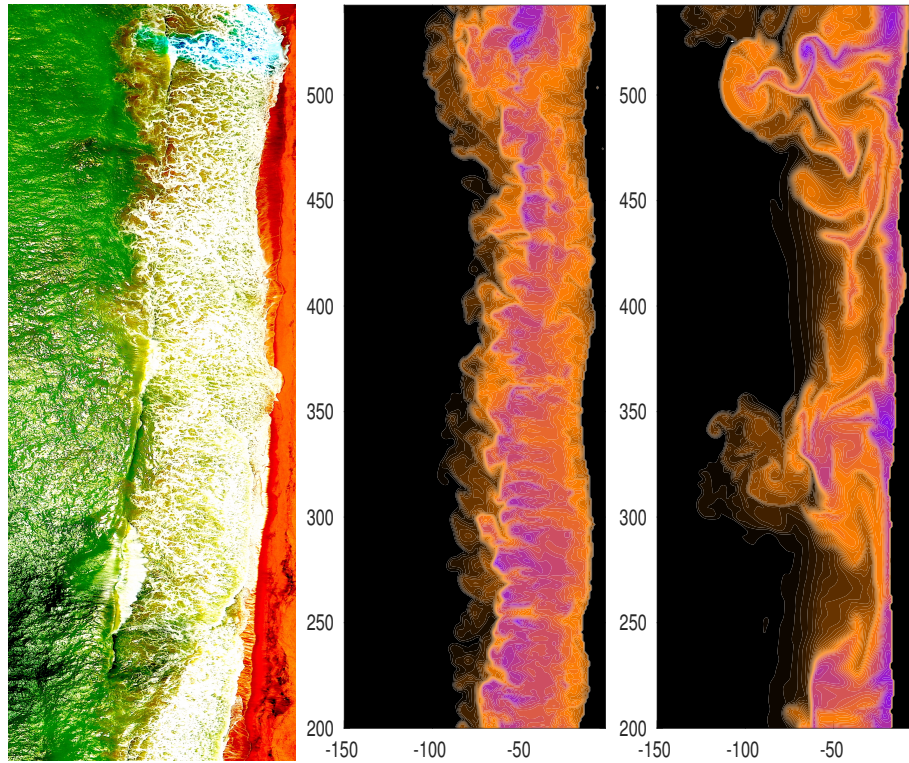


Figure 10: Aerial photo (left) and CROCO simulations of surfzone suspended sediments for shallow-breaking (center) and deep-breaking (right) cases. The contrasts in the photo is enhanced to better expose suspended sediments (brown color). The model suspended sediments correspond to snapshots at 15 min of simulation.

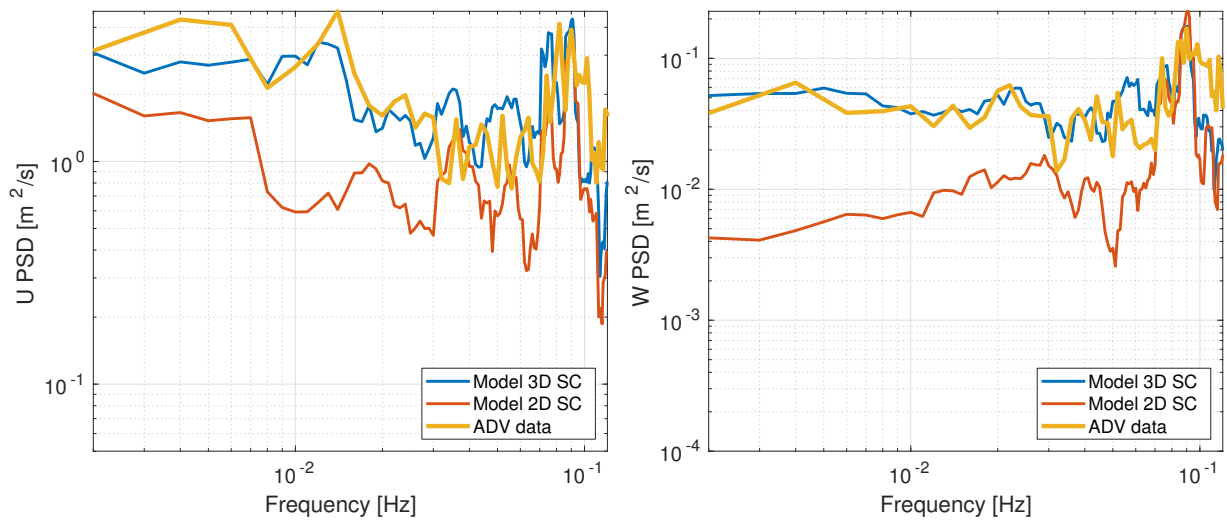


Figure 11: Power Spectral Density of horizontal (left) and vertical (right) velocity fluctuations compared with ADV measurements in the middle of the terrace, in March 13 2014 at afternoon mid-tide.

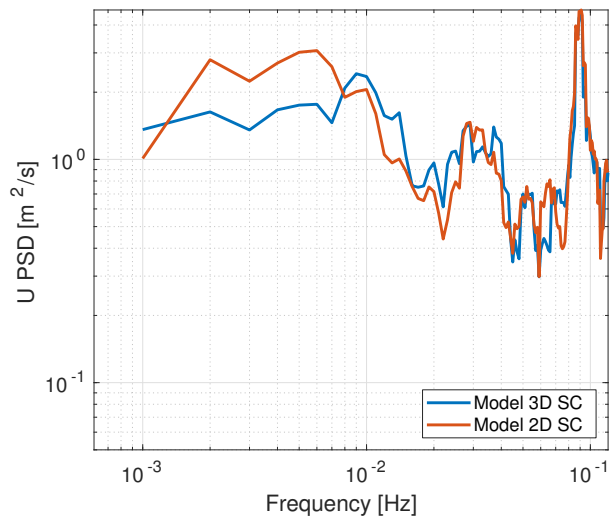


Figure 12: Power Spectral Density of offshore horizontal velocity fluctuations in March 13 2014 at afternoon mid-tide.

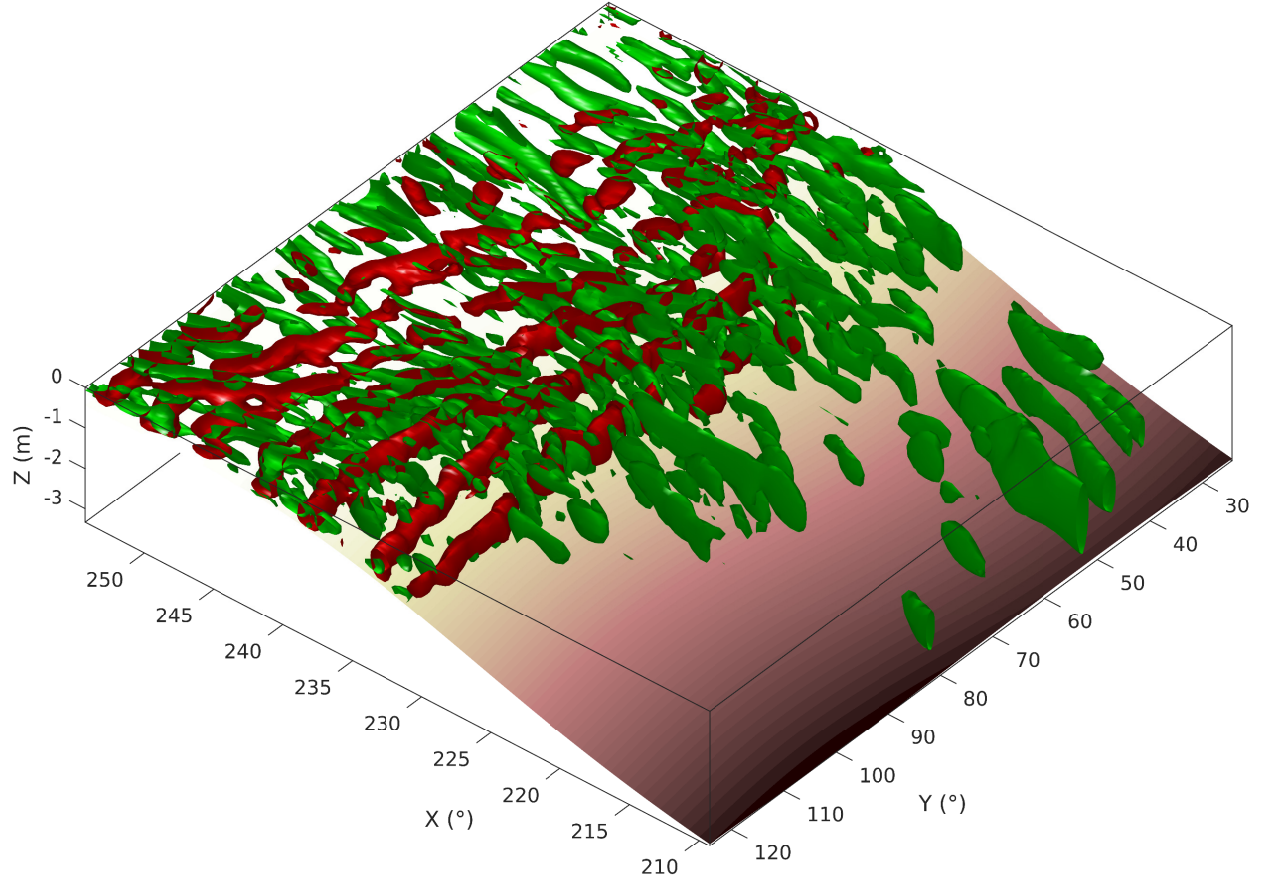


Figure 13: Q field defined by $Q = -\frac{1}{2} \frac{\partial u_i}{\partial x_j} \frac{\partial u_j}{\partial x_i}$, showing coherent structures similar to rolls and ribs in a transitional mixing layer. Cross-shore and alongshore Q terms are split: spanwise rolls (aligned across shear direction) are identified by $Q_y = -\frac{\partial u}{\partial z} \frac{\partial w}{\partial x} - \frac{1}{2} \frac{\partial u^2}{\partial x}$ in red; and streamwise ribs (along shear direction) are identified by $Q_x = -\frac{\partial v}{\partial z} \frac{\partial w}{\partial y} - \frac{1}{2} \frac{\partial v^2}{\partial y}$ in green. The fields are normalized and only positive isosurface values (0.02) are plotted.

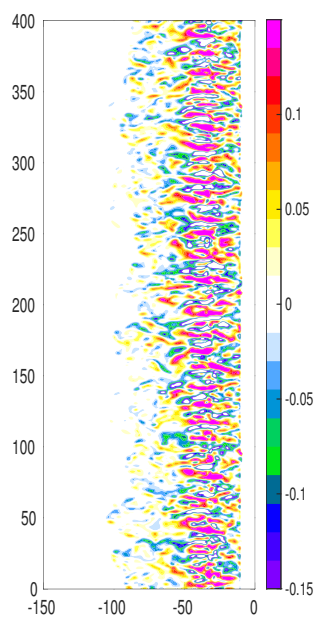


Figure 14: Vertical vorticity snapshot for the case with monochromatic shore-normal wave forcing (3D_MONO_D0)

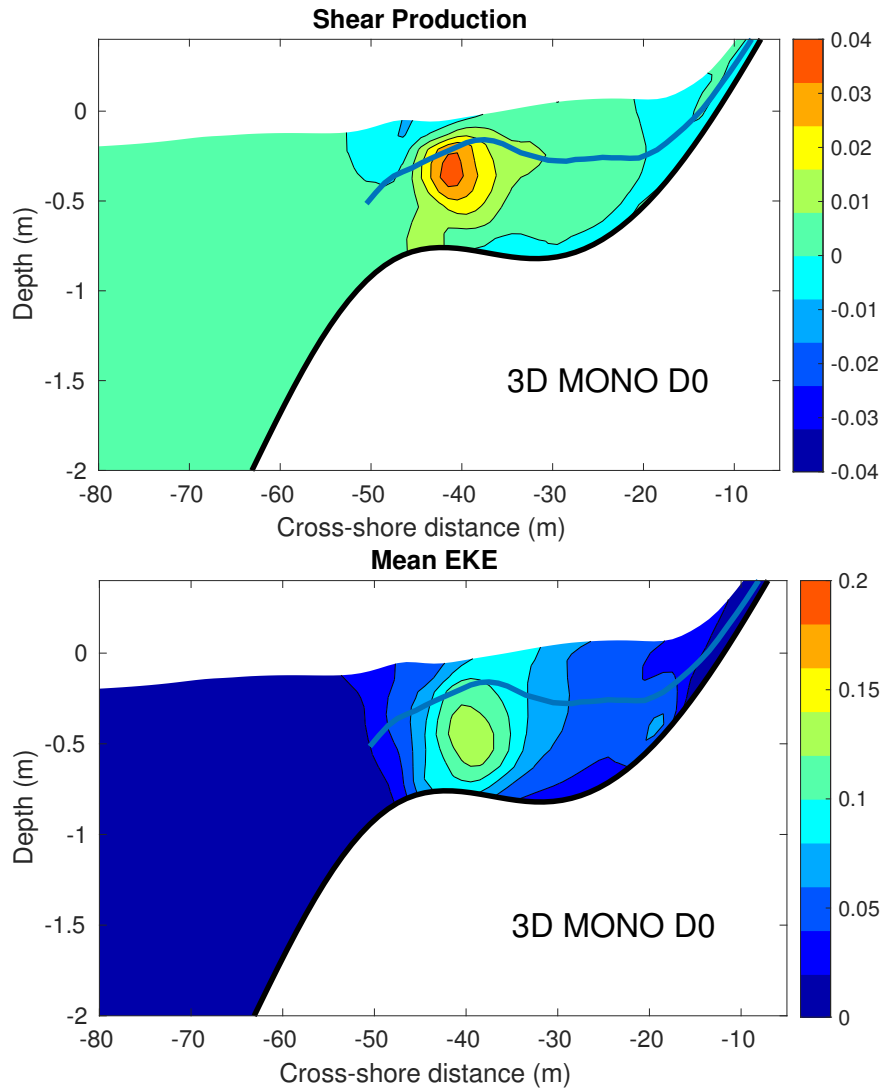


Figure 15: Cross-section of EKE [m^2/s^3] (bottom) and EKE production by the mean shear flow (top) [m^2/s^3] for the case with 3D instabilities only, forced with monochromatic long-crested waves (3DMONOD0). The position of shear flow inflection point is drawn in a blue line

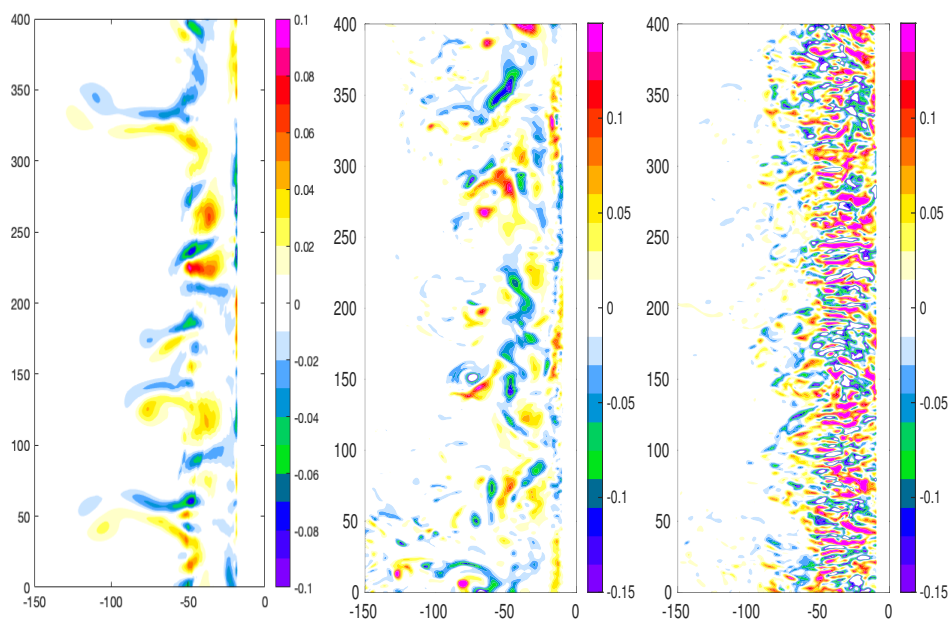


Figure 16: Vertical vorticity snapshot for 3 cases with shore-normal wave forcing: FUNWAVE-TVD (2D Boussinesq) with short-crested waves (left); CROCO with short-crested waves and deep breaking (center); short-crested waves and shallow breaking (right).

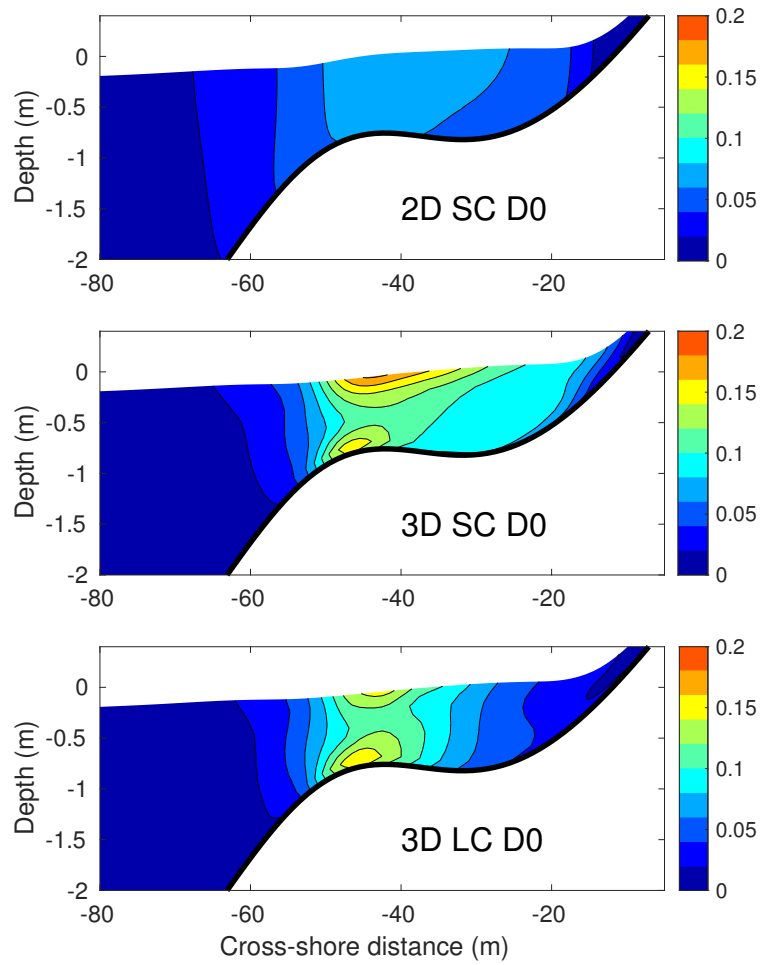


Figure 17: Cross-section of time-mean and longshore-mean EKE for the 3 cases of Figure 16

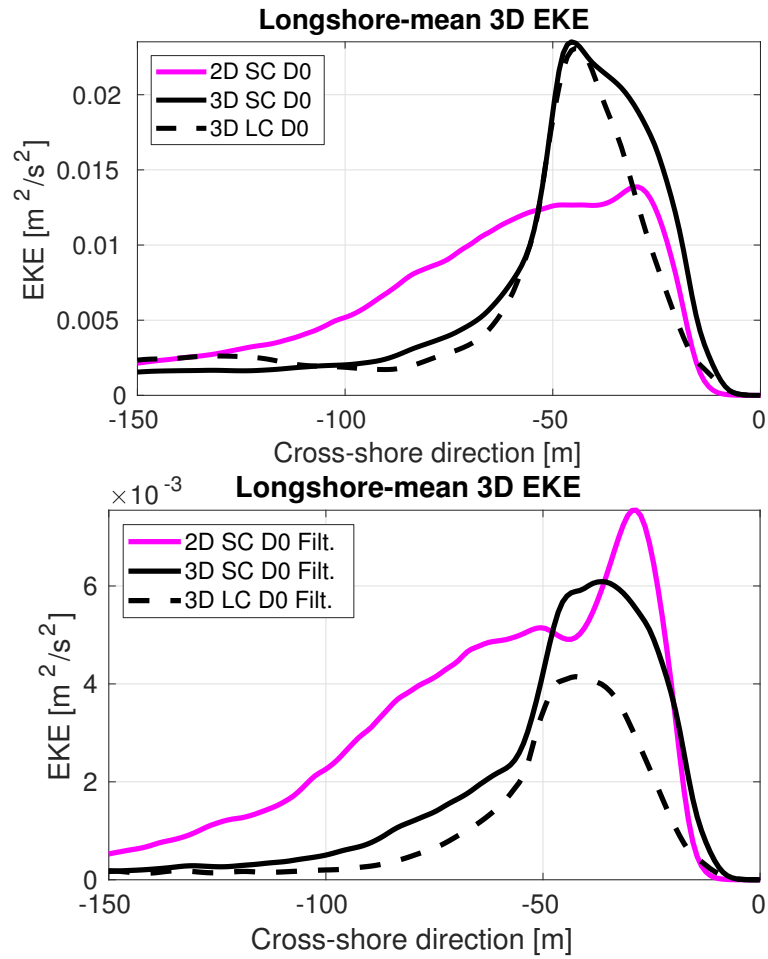


Figure 18: Cross-shore profile of depth-integrated (normalized), time and longshore-mean EKE for the 3 cases in Figure 16. Top: EKE of wave-averaged flow; bottom: EKE of low-pass filtered flow to remove 3D instability modes.

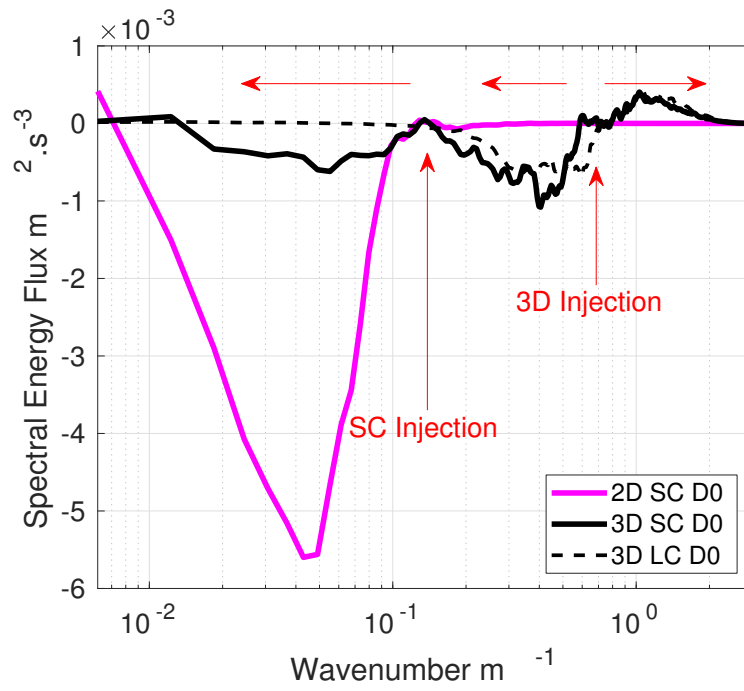


Figure 19: 3D and 2D model wavenumber spectral flux in the surfzone. Vertical red arrows point to the wavenumbers of energy injection from short-crested waves (~ 40 m wavelength) and from 3D shear instability (~ 10 m). The spectral flux is computed by spectral integration of v advection term (Marchesiello et al., 2011). Horizontal red arrows indicate positive/negative fluxes, i.e., direct/inverse energy cascade toward smaller/larger scales.

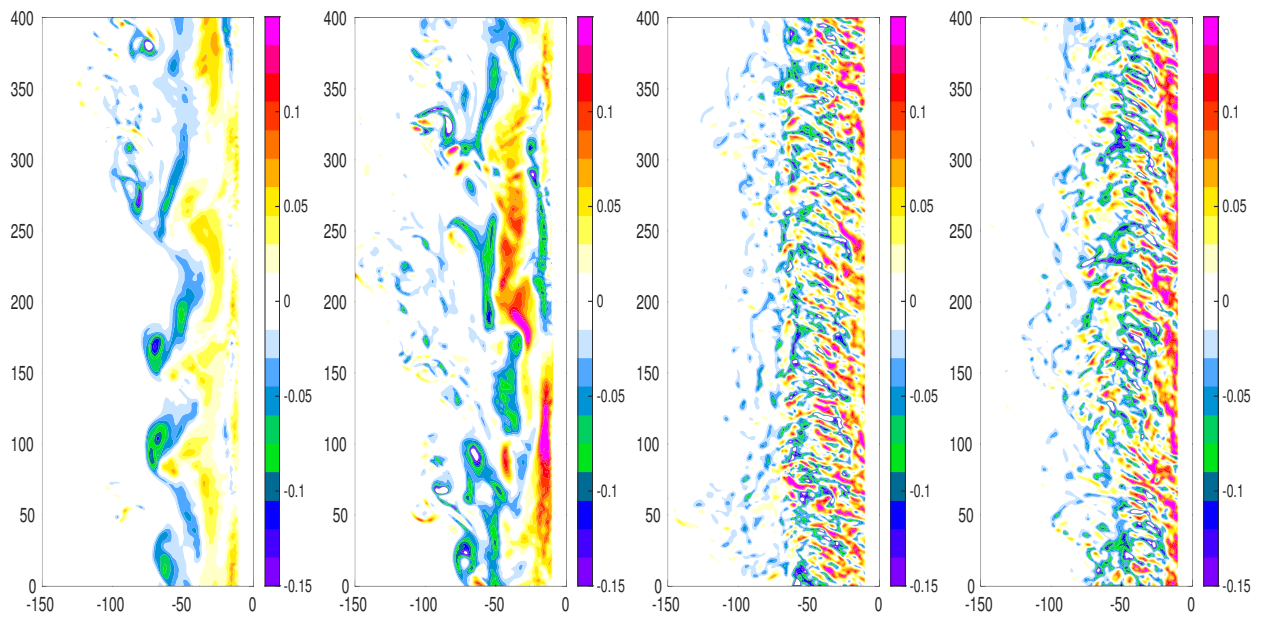


Figure 20: Snapshot of vorticity fields for 4 cases with oblique waves: long-crested waves with deep breaking (2D_LC_D20: first left); short-crested waves with deep breaking (2D_SC_D20: second left); long-crested waves with shallow breaking (3D_LC_D20: first right) and short-crested waves with shallow breaking (3D_SC_D20: last right).

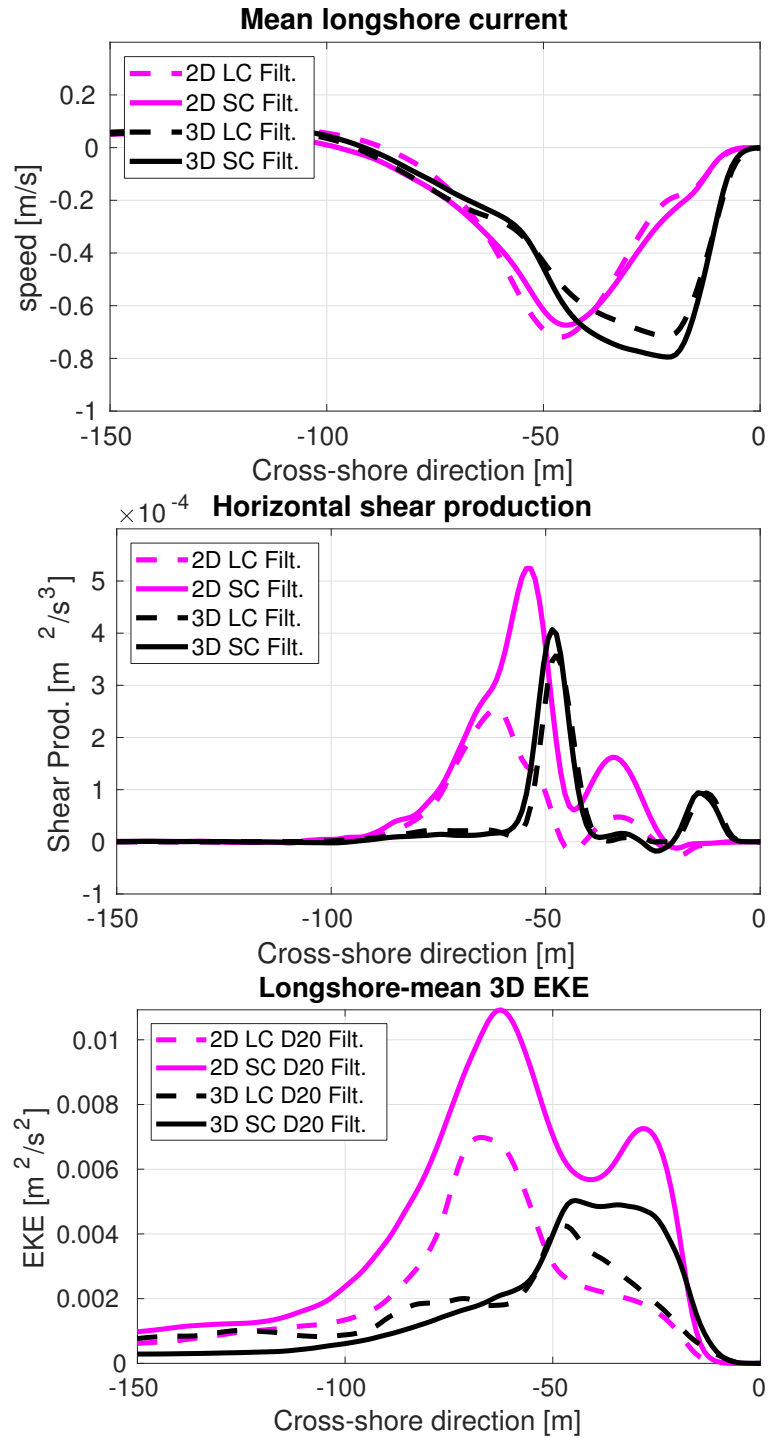


Figure 21: Cross-shore profile of time-mean and longshore-mean flow and eddy statistics for the 4 cases in Figure 16; top) surface longshore flow; center): horizontal shear production $-\overline{u'v'}\frac{\partial \bar{v}}{\partial x}$; bottom) depth-integrated (normalized) EKE (computed from low-pass filtered velocities showing low-frequency modes).